# Buckling of thermally fluctuating spherical shells: Parameter renormalization and thermally activated barrier crossing

Lorenz Baumgarten and Jan Kierfeld

Phys. Rev. E **97**, 052801 — Published 4 May 2018

DOI: 10.1103/PhysRevE.97.052801

# Buckling of thermally fluctuating spherical shells: parameter renormalization and thermally activated barrier crossing

Lorenz Baumgarten* and Jan Kierfeld†

*Physics Department, TU Dortmund University, 44221 Dortmund, Germany*
(Dated: April 19, 2018)

We study the influence of thermal fluctuations on the buckling behavior of thin elastic capsules with spherical rest shape. Above a critical uniform pressure, an elastic capsule becomes mechanically unstable and spontaneously buckles into a shape with an axisymmetric dimple. Thermal fluctuations affect the buckling instability by two mechanisms. On the one hand, thermal fluctuations can renormalize the capsule's elastic properties and its pressure because of anharmonic couplings between normal displacement modes of different wavelengths. This effectively lowers its critical buckling pressure [A. Košmrlj and D.R. Nelson, Phys. Rev. X **7**, 011002 (2017)]. On the other hand, buckled shapes are energetically favorable already at pressures below the classical buckling pressure. At these pressures buckling requires, however, to overcome an energy barrier, which only vanishes at the critical buckling pressure. In the presence of thermal fluctuations the capsule can spontaneously overcome an energy barrier of the order of the thermal energy by thermal activation already at pressures below the critical buckling pressure. We revisit parameter renormalization by thermal fluctuations and formulate a new buckling criterion based on scale-dependent renormalized parameters to obtain a temperature-dependent critical buckling pressure. Then we quantify the pressure-dependent energy barrier for buckling below the critical buckling pressure using numerical energy minimization and analytical arguments. This allows us to obtain the temperature-dependent critical pressure for buckling by thermal activation over this energy barrier. Remarkably, both parameter renormalization and thermal activation lead to the same parameter dependence of the critical buckling pressure on temperature, capsule radius and thickness, and Young's modulus. Finally, we study the combined effect of parameter renormalization and thermal activation by using renormalized parameters for the energy barrier in thermal activation to obtain our final result for the temperature-dependent critical pressure, which is significantly below the results if only parameter renormalization or only thermal activation is considered.

## I. INTRODUCTION

Elastic capsules are thin-walled elastic shells enclosing a fluid medium. Bending energy penalizes deviations in curvature from a specific spontaneous curvature, and two-dimensional elastic energy penalizes stretching and shear deformations of the quasi two-dimensional solid shell with respect to a reference or rest shape, in which the capsule is stress-free.

On the microscale, there are many biological examples of elastic capsules such as red blood cells [1, 2], virus capsids [3, 4], and pollen grains [5]. Microcapsules can also be artificially produced by various methods, e.g., as hollow polymer or polyelectrolyte capsules [6–8]. Both biological and artificial microcapsules are typically used to encapsulate, transport, and eventually release a substance. Artificial elastic capsules are used as container and delivery systems in numerous applications, such as food technology [9], cosmetics [10], chemical industry, and pharmacy [11, 12]. Also, all macroscopic elastic shells (such as beach balls, egg shells, etc.) are described by the same continuum shell elasticity as microcapsules.

Often the capsule's reference shape is a sphere (of radius $R_0$). A notable exception are red blood cells, where the reference shape is an oblate spheroid [1]. If the capsule material can be viewed as a thin shell of thickness $h$ ($\ll R_0$) made from an isotropic and homogeneous elastic material, the shell has a bending modulus $\kappa \propto h^3$ but a two-dimensional Young's modulus $Y \propto h$ [13, 14]. Therefore, bending deformations are energetically preferred over stretching or shear deformations for thin shells. Very thin elastic capsules therefore exhibit a peculiar deformation behavior. In the extreme case of an infinitely thin shell, only isometric deformations, i.e., deformations that preserve the metric and, thus, the Gaussian curvature and the stretching and shear energies, are possible. There is, however, no smooth and isometric deformation of spheres or ellipsoids, which makes elastic capsules quite resistant to pressure or volume decrease, creating a "geometry-induced rigidity" in thin capsules [15, 16], which is also employed on the macroscale for mechanical stability of dome-like structures.

This rigidity makes elastic capsules stable under a uniform external pressure, and, for small pressures, they retain their spherical shape. Above a critical pressure, however, a buckling instability occurs, where the spherical shape becomes mechanically unstable and a dimple is finally formed [13, 17]. Understanding the buckling instability is both important from a structural mechanics perspective, as it is relevant for the mechanical stability of macroscopic spherical shells, and in the context of microcapsules, which can buckle, for example, by osmotic

* lorenz.baumgarten@tu-dortmund.de
† jan.kierfeld@tu-dortmund.de

pressure [18–21]. Following Pogorelov [22], the dimple can be viewed as an approximative inverted spherical cap whose sharp edge at the rim is rounded to avoid infinite bending energies. Such a rounded spherical cap is, therefore, an approximative isometry of the spherical rest shape, which avoids large stretching energies.

For ideal spherical shells the classical buckling pressure $p_c$ has been known for more than 100 years [23]. For a shell with rest radius $R_0$, bending rigidity $\kappa$, 2D Young's modulus $Y$, one finds [17, 24]

$$p_c = 4\frac{\sqrt{Y\kappa}}{R_0^2} = 4\frac{Eh^2}{R_0^2\sqrt{12(1-\nu^2)}} = 4\frac{Y}{R_0}\gamma^{-1/2}. \quad (1)$$

The second equality applies for thin shells of thickness $h$ made from an isotropic elastic material with bulk Young modulus $E$ and Poisson ratio $\nu$, where $\kappa = Eh^3/12(1-\nu^2)$ and $Y = Eh$ [24]. We also introduced the Föppl-von Kármán number

$$\gamma \equiv \frac{YR_0^2}{\kappa} = 12(1-\nu^2)\left(\frac{R_0}{h}\right)^2, \quad (2)$$

which is an inverse dimensionless bending rigidity. The ideal critical pressure $p_c$ is, however, not reached in experiments on macroscopic shells, because imperfections reduce the buckling pressure significantly. Such imperfections have been discussed by Hutchinson [25] and Koiter [26] in the form of additional quenched normal displacements.

At $p_c$ (or a $p_c$ reduced by imperfections) buckling occurs as an instability with respect to oscillatory normal displacements, the shortest possible wavelength of which is $\lambda_c = 2\pi R_0\gamma^{-1/4} = 2l_{\rm el}$ [25], which sets an important elastic length scale

$$l_{\rm el} \equiv \pi\left(\frac{\kappa R_0^2}{Y}\right)^{1/4} = \frac{12^{1/4}\pi}{(1-\nu^2)^{1/4}}\sqrt{R_0 h} = \pi R_0\gamma^{-1/4} \quad (3)$$

in the buckling problem. For thin shells with $\gamma \gg 1$, the buckling wavelength is small compared to the shell radius (but large compared to shell thickness). There are many unstable modes with this wavelength, and the buckling instability results in a hexagonal lattice of dimples of size $\sim \lambda_c$ on the sphere, as was shown theoretically [25, 26] and also by experiments [27] and numerical simulations [28]. This buckling pattern is unstable with respect to growth of one of the dimples on the expense of the others, finally resulting in a single axisymmetric dimple. For a fixed mechanical pressure $p \geq p_c$, the dimple will actually snap through and grow until opposite sides are in contact, whereas for osmotic pressure control or even volume control, a stable dimple shape is reached before opposite sides come into contact [29, 30]. The dimple can, however, assume a polygonal shape in a *secondary* buckling transition [31–33].

Interestingly, the buckled state with a single axisymmetric dimple becomes *energetically* favorable already at a much lower pressure $p_{c1} \ll p_c$, which is sometimes also called *Maxwell pressure* because it can be obtained from a Maxwell construction of equal energies [29, 30, 34, 35]. For $p_c > p > p_{c1}$, the axisymmetrically buckled configuration with a single dimple has a lower energy as compared to a spherical shape, but the spherical shape remains a local energy minimum, which is protected by an *energy barrier* from buckling [29, 30]. [36] For mechanical pressure control, a parameter dependence

$$p_{c1} \sim p_c\gamma^{-1/4} \sim \frac{Y}{R_0}\gamma^{-3/4} \sim \frac{Eh^{5/2}}{R_0^{5/2}} \quad (4)$$

has been found [30]. The results of Ref. [29] show that there is also a critical *unbuckling pressure* $p_{\rm cu}$, below which no stable buckled shape exists. In Ref. [37], $p_{\rm cu} \sim 3p_{c1}/4$ has been found, i.e., $p_{\rm cu}$ has the same parameter dependence as $p_{c1}$. The unbuckling pressure also corresponds to the minimum pressure on the pressure-volume relation of the buckled branch, for which the same parameter has been found in Refs. [35, 38].

As a result, there is a rather wide pressure window $p_c > p > p_{c1}$, where buckling is energetically possible but must be induced by imperfections or other external perturbations because an energy barrier has to be overcome. This energy barrier has been subject of a number of recent studies both for spherical [34, 35, 39–41] and cylindrical [41, 42] shells and will be quantified in this paper for spherical shells by numerical calculations. One important cause of perturbation to be studied within this work and particularly relevant for thin shells or capsules are thermal fluctuations. Thin shells or two-dimensional elastic materials deform easily by bending and can therefore exhibit pronounced thermal shape fluctuations at room temperature [43]. Thermal fluctuations could give rise to thermal activation over the buckling energy barrier. Fig. 1 shows that both experimental values for macroscopic shells as well as simulation results for thermally fluctuating shells always lie within the pressure window $p_c > p > p_{c1}$, where buckling is energetically allowed.

This suggests that thermal fluctuations of a shell or capsule can have two effects on the buckling transition: (i) They induce shape fluctuations similar to the imperfections studied in Refs. [25, 26]. Therefore, they should *reduce* the classical buckling pressure $p_c$ where a spontaneous mechanical instability sets in. (ii) They give rise to thermal activation over the buckling energy barrier in the pressure window between $p_c$ and $p_{c1}$, which leads to a further reduction of the apparent buckling pressure $p_c$ in the presence of thermal fluctuations.

The effect (i) has already been studied analytically and numerically in Refs. [44, 45]. Using renormalization group (RG) calculations, it has been established that thermal shape fluctuations of a shell renormalize its Young modulus downwards and bending rigidity upwards and generate an effective compressive pressure [45]. As a result, the classical buckling pressure is *decreased* by thermal shape fluctuations, i.e., the shell effectively softens and becomes increasingly unstable with temperature,

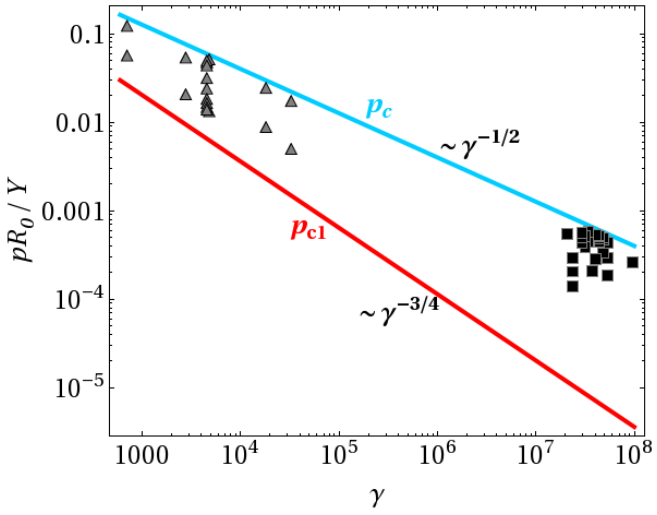


FIG. 1. Classical buckling pressure $p_c \propto \gamma^{-1/2}$ (dark red line) and critical pressure $p_{c1} \propto \gamma^{-3/4}$ (light blue line), where buckling is already energetically favorable according to Ref. [30]. Experimental results (black squares, from Ref. [27]) and finite-temperature Monte Carlo simulations (grey triangles, from Ref. [44]) for the buckling pressure lie between $p_c$ and $p_{c1}$.

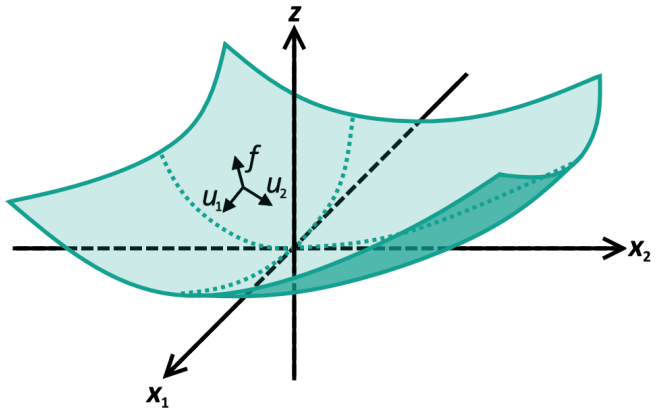


FIG. 2. Coordinate System used in the shallow shell theory.

which has also been observed in Monte-Carlo simulations of thermally fluctuating shells [44]. Using the same RG treatment as Ref. [45] but different buckling criteria, we will arrive at essentially the same conclusions.

The effect (ii) of thermal activation over the buckling energy barrier has not been considered so far and is the main subject of the present paper. First we will quantify the pressure-dependent buckling energy barrier $F_{\rm B}$ using numerical energy minimization. We find a scaling behavior $F_{\rm B}(p) \sim Y R_0^2 \gamma^{-3/2} f_p\,(p/p_c) \sim (Eh^4/R_0) f_p\,(p/p_c)$ of the buckling energy barrier with a scaling function $f_p(x) \sim (1-x)^2 x^{-3}$. Then we consider the sole effect of thermal activation without parameter renormalization and calculate an apparent buckling pressure from arguing that, at a finite temperature, energy barriers of the size of the thermal energy $k_BT$ ($k_B$ is the Boltzmann constant and $T$ temperature) can be overcome quasi-spontaneously on experimental time scales by thermal activation. Finally, we will study the combined effect of (i) parameter renormalization and (ii) thermal activation and find a further reduction of the apparent critical buckling pressure both below the results if only parameter renormalization or only thermal activation is considered.

We can compare our results to existing numerical Monte-Carlo simulation results [44], which show that, for $T > 0$, the critical buckling pressure $p_c(T)$ is only weakly decreasing with temperature for $k_BT < \kappa/\sqrt{\gamma}$ but exhibits a pronounced decrease for $k_BT > \kappa/\sqrt{\gamma}$. The simulation data could be collapsed onto a curve $p_c(T)/p_c(0) = f(k_BT\sqrt{\gamma}/\kappa)$, where $f(x)$ is a scaling function. We will obtain the same scaling of the critical buckling pressure with $k_BT\sqrt{\gamma}/\kappa$ *both* for (i) parameter renormalization *and* (ii) thermal activation because $F_B(p) \sim \kappa/\sqrt{\gamma} f_p\,(p/p_c)$.

## II. BUCKLING AND PARAMETER RENORMALIZATION

We start by recapitulating the RG approach of Refs. [44, 45] leading to the RG transformation for the scale-dependent elastic moduli and a scale-dependent pressure. Based on these RG equations we discuss several buckling criteria, which are slightly different from those used in Ref. [45] but give rise to very similar temperature-dependent buckling pressures.

### A. Elastic energy and thermal fluctuations

The elastic energies of a spherical shell or capsule can be calculated using shallow shell theory [26], which is accurate for weakly curved shells with $h \ll R_0$ or, alternatively, at large Föppl-von Kármán numbers $\gamma = YR_0^2/\kappa \gg 1$ [see Eq. (2)]. In shallow shell theory, the undeformed reference state of a nearly flat section of the sphere is described by a height function $Z(\mathbf{x})$, where the Cartesian coordinates $\mathbf{x} = (x_1, x_2)$ define a tangent plane that touches the sphere at the origin as shown in Fig. 2. For a spherical shell the reference state has constant mean curvature $1/R_0$.

The reference state is deformed by tangential displacements $\mathbf{u}(\mathbf{x})$ ($\mathbf{u} = (u_1, u_2)$) and normal displacements $f(\mathbf{x})$ ($f > 0$ shall correspond to inward displacements), see Fig. 2. For small displacements of the spherical reference shape, we obtain a strain tensor [13]

$$u_{ij} = \frac{1}{2}(\partial_i u_j + \partial_j u_i + \partial_i f \partial_j f) - \delta_{ij}\frac{f}{R_0} \qquad (5)$$

and a corresponding in-plane elastic energy

$$E_S = \frac{1}{2}\int \mathrm{d}S(2\mu u_{ij}^2 + \lambda u_{kk}^2), \tag{6}$$

with the Lamé coefficients $\mu$ and $\lambda$ and the area element $\mathrm{d}S$.

For the bending energy, we can use the Helfrich form [46] (assuming $\nu = 1$ for bending [29]),

$$E_b = \frac{\kappa}{2}\int \mathrm{d}S(2H - 2H_0)^2, \tag{7}$$

where $\kappa$ is the bending rigidity, $H$ the mean curvature, and $H_0 = 1/R_0$ the spontaneous mean curvature of the undeformed sphere. For a shallow section of the shell, the mean curvature can be written as

$$2H = \nabla^2(Z + f) = \frac{2}{R_0} + \nabla^2 f,$$

where $\nabla^2 = \partial_{11} + \partial_{22}$.

Adding the mechanical work by an external pressure $p$ (with the sign convention that $p > 0$ is a compressive pressure), the total enthalpy is

$$\begin{aligned} F &= E_S + E_b - p\int \mathrm{d}S f \\ &= \int \mathrm{d}^2x \left[\frac{\kappa}{2}\left(\nabla^2 f\right)^2 + \mu u_{ij}^2 + \frac{\lambda}{2}u_{kk}^2 - pf\right]. \end{aligned} \tag{8}$$

The strain tensor (5) contains terms $\partial_i f \partial_j f$ and the coupling $f/R_0$ of normal displacements to the Gaussian background curvature, both of which give rise to anharmonicities in the normal displacement field $f$ in the enthalpy. The latter source of anharmonicities is characteristic for bent shells and vanishes in the limit $R_0 \to \infty$ of a planar plate or membrane. The free enthalpy $G$ is obtained by integrating out all thermal displacement fluctuations, $G = -k_BT \ln\left[\int \mathcal{D}\mathbf{u} \int \mathrm{d}f e^{-F/k_BT}\right]$, which can not be achieved analytically in explicit form because of the anharmonicities. In a RG calculation this integration is performed iteratively, starting from small scales, and contributions from anharmonicities are absorbed into renormalized scale-dependent elastic moduli $\kappa_R$ and $Y_R$ and a scale-dependent renormalized pressure $p_R$.

To this end, the normal displacement is separated into a uniform part $f_0$ caused by the homogeneous pressure $p$ and a nonuniform part $\tilde{f}(\mathbf{x})$ solely due to thermal fluctuations,

$$f(\mathbf{x}) = f_0 + \tilde{f}(\mathbf{x}) = f_0 + \sum_{\mathbf{q}\neq 0} \tilde{f}(\mathbf{q}) e^{-i\mathbf{q}\cdot\mathbf{x}}, \tag{9}$$

with Fourier components $\tilde{f}(\mathbf{q}) = A^{-1}\int \mathrm{d}^2x f(\mathbf{x}) e^{i\mathbf{q}\cdot\mathbf{x}}$, where $A$ is the area in the $\mathbf{x}$-plane. The enthalpy $F$ is split into a harmonic and an anharmonic part. Only the uniform normal displacement contributes to the pressure term, and only the nonuniform term contributes to the nonlinear part of the strain tensor. Therefore, the enthalpy is harmonic in $u_i(\mathbf{x})$ and $f_0$, and these fields are eliminated by defining an effective enthalpy [47]

$$F_{\mathrm{eff}}[\tilde{f}] = -k_BT \ln\left[\int \mathcal{D}\mathbf{u} \int \mathrm{d}f_0 e^{-F/k_BT}\right]. \tag{10}$$

Integrating out the phonon fields $u_i$ and homogeneous modes $f_0$, we obtain [44]

$$\begin{aligned} F_{\mathrm{eff}}[\tilde{f}] = \int \mathrm{d}^2x \Bigg(&\frac{1}{2}\left[\kappa\left(\nabla^2\tilde{f}\right)^2 - \frac{pR_0}{2}|\nabla\tilde{f}|^2 + \frac{Y\tilde{f}^2}{R_0^2}\right] \\ &+ \frac{Y}{8}\left[P_{ij}^T(\partial_i\tilde{f})(\partial_j\tilde{f})\right]^2 - \frac{Y\tilde{f}}{2R_0}\left[P_{ij}^T(\partial_i\tilde{f})(\partial_j\tilde{f})\right]\Bigg), \end{aligned} \tag{11}$$

(we sum over double indices) where $P_{ij}^T = \delta_{ij} - \partial_i\partial_j/\nabla^2$ is the transverse projection operator and $Y = 4\mu(\mu + \lambda)/(2\mu + \lambda)$ is 2D Young's modulus. The last cubic term is characteristic for bent shells and vanishes in the limit $R_0 \to \infty$ of a planar plate or membrane. Appearance of a cubic term simply reflects a missing mirror symmetry for bent shells.

The corresponding Fourier transformed correlation function $G(\mathbf{q}) \equiv \langle|\tilde{f}(\mathbf{q})|^2\rangle$ is in harmonic approximation [44]

$$G_0(\mathbf{q}) = \frac{k_BT}{A\left[\kappa q^4 - \frac{1}{2}pR_0q^2 + \frac{Y}{R_0^2}\right]}. \tag{12}$$

In the RG approach anharmonic contributions are absorbed into scale-dependent renormalized parameters $\kappa_R(q)$, $p_R(q)$, and $Y_R(q)$ that replace $\kappa$, $p$, and $Y$ in (12) such that the full correlation function shall finally be obtained in the form

$$G(\mathbf{q}) = \frac{k_BT}{A\left[\kappa_R(q)q^4 - \frac{1}{2}p_R(q)R_0q^2 + \frac{Y_R(q)}{R_0^2}\right]}. \tag{13}$$

### B. Renormalization Group Transformation

Now, we shortly recapitulate the derivation of the scale-dependent parameters $\kappa_R(q)$, $p_R(q)$, and $Y_R(q)$ by Košmrlj and Nelson [45]. In the RG transformation, fluctuations in the normal displacement field $\tilde{f}$ are integrated out up to the length scale $l = ab$ or down to a wave number $q = \pi/l = \Lambda/b$, where $b = e^s$ is the scale factor of the RG transformation and $a = \pi/\Lambda$ is a microscopic cutoff scale (e.g., the shell thickness). Košmrlj and Nelson have shown that the exact choice of $a$ is irrelevant as long as $a \ll l_{\mathrm{el}}$, with the *elastic length scale* (3), which is the length scale of initial dimples at the classical buckling instability, and $a \ll l_{\mathrm{th}}$, with the *thermal length scale* $l_{\mathrm{th}} \equiv \sqrt{16\pi^3\kappa^2/3k_BTY}$, which is the length scale above which thermal fluctuations become relevant

for flat plates. After integrating out, the original cutoff is re-established by rescaling lengths and fields according to

$$\mathbf{x} = b\mathbf{x}' \ , \quad \mathbf{q} = b^{-1}\mathbf{q}' \ , \quad \tilde{f}(\mathbf{q}) = b^{\zeta_f}\tilde{f}'(\mathbf{q}'), \tag{14}$$

with a field rescaling exponent $\zeta_f$.

In a momentum shell RG approach, the normal displacements $\tilde{f}$ are separated into slow modes $\tilde{f}_<(\mathbf{x}) = \sum_{|\mathbf{q}|<\Lambda/b} e^{i\mathbf{q}\cdot\mathbf{x}}\tilde{f}(\mathbf{q})$ and fast modes $\tilde{f}_>(\mathbf{x}) = \sum_{|\mathbf{q}|>\Lambda/b} e^{i\mathbf{q}\cdot\mathbf{x}}\tilde{f}(\mathbf{q})$ containing modes with wave numbers smaller and larger than $\Lambda/b$, respectively. We integrate over modes $\tilde{f}_>$ in the momentum shell $\Lambda/b < |\mathbf{q}| < \Lambda$ to obtain an effective enthalpy for the slow modes $\tilde{f}_<$,

$$F'_{\rm eff}[\tilde{f}_<] = -k_BT \ln\left(\int \mathcal{D}[\tilde{f}_>(\mathbf{x})] e^{-F_{\rm eff}/k_BT}\right).$$

Then we rescale lengths and fields according to Eq. (14). The effective enthalpy for slow modes retains its form (11) by this change of scale by a factor $b$ if new renormalized elastic parameters $\kappa'(s)$, $Y'(s)$, and $p'(s)$ are introduced. Their RG flow for an infinitesimal change of scale $b \approx 1 - ds$ is described by $\beta$-functions

$$\beta_\kappa = \frac{{\rm d}\kappa'}{{\rm d}s} = 2(\zeta_f - 1)\kappa' + \frac{3k_BTY'\Lambda^2}{16\pi D} - \frac{3k_BTY'^2\Lambda^2}{8\pi R_0'^2 D^2}\left[\frac{11}{12} + \frac{I_{\kappa 1}}{D^2} + \frac{I_{\kappa 2}}{D^4}\right], \tag{15a}$$

$$\beta_Y = \frac{{\rm d}Y'}{{\rm d}s} = 2\zeta_f Y' - \frac{3k_BTY'^2\Lambda^6}{32\pi D^2}, \tag{15b}$$

$$\beta_p = \frac{{\rm d}p'}{{\rm d}s} = (2\zeta_f + 1)p' + \frac{3k_BTY'^2\Lambda^4}{4\pi R_0'^3 D^2}\left[1 + \frac{I_p}{D^2}\right], \tag{15c}$$

$$\beta_R = \frac{{\rm d}R_0'}{{\rm d}s} = -R_0', \tag{15d}$$

where the denominator

$$D \equiv \kappa'\Lambda^4 - \frac{p'R_0'\Lambda^2}{2} + \frac{Y'}{R_0'^2} \tag{16}$$

was introduced. The terms $I_{\kappa 1}$, $I_{\kappa 2}$, and $I_p$ are given in Eq. (A11) in Appendix A. The function $\beta_\kappa$ (15a) seemingly differs in two terms from the results of Ref. [45] but is actually identical. For a consistent renormalization of the three- and four-point vertices, we choose $\zeta_f = 1$.

Finally, the scale-dependent quantities $\kappa_R(q)$, $p_R(q)$, and $Y_R(q)$, in terms of which the full correlation function (13) can be written, are obtained by undoing the rescaling operation; this gives (using $\zeta_f = 1$)

$$\kappa_R(q) = \kappa'(s)e^{(2-2\zeta_f)s} = \kappa'(s), \tag{17a}$$

$$Y_R(q) = Y'(s)e^{-2\zeta_f s} = Y'(s)e^{-2s}, \tag{17b}$$

$$p_R(q) = p'(s)e^{(-1-2\zeta_f)s} = p'(s)e^{-3s}, \text{ and} \tag{17c}$$

$$R_{0,R}(q) = R_0'(s)e^s = R_0, \tag{17d}$$

where $s = s(q)$ is given by $e^s = \Lambda/q$. These parameters arise by simply integrating out fluctuations up to the scale $\ell = \pi/q = ae^s$, i.e., modes with wave numbers $> q$, *without* subsequent rescaling and obey the RG equations (A12) given in the Appendix. For any other quantity, the index "R" also indicates that it is a scale-dependent, i.e., renormalized but unrescaled quantity.

### C. Buckling criteria

The classical buckling instability at the pressure $p_c = 4\sqrt{Y\kappa}/R_0^2$ [see Eq. (1)] manifests in the presence of thermal fluctuations as the smallest pressure where the denominator $\kappa q^4 - \frac{1}{2}pR_0q^2 + Y/R_0^2$ of the correlation function $G_0(\mathbf{q})$ in harmonic approximation from Eq. (12) can become zero, which happens at the wave number $q_{\rm el} = (p_cR_0/4\kappa)^{1/2} = (Y/\kappa R_0^2)^{1/4} = \pi/l_{\rm el}$ [see Eq. (3)], which indeed corresponds to the wavelength $\lambda_c$ of the classical buckling instability. At this point the shell becomes energetically unstable with respect to small fluctuations in the radial deformation mode $\tilde{f}(q_c)$, which initiates the buckling transition.

In the presence of thermal fluctuations, elastic constants and pressure are renormalized according to (15) and become dependent on the length scale $\ell \sim 1/q$ up to which fluctuations have been integrated out: $\kappa_R(q)$ grows, $Y_R(q)$ decreases, and also the pressure $p_R(q)$ grows for decreasing $q$ or increasing length scales $\ell$. At $T > 0$ buckling happens analogously to the mechanical $T = 0$ case if the denominator of the correlation function $G(q)$ (the two-point vertex function),

$$D_R(q) \equiv k_BT/AG(q) = \kappa_R(q)q^4 - \frac{1}{2}p_R(q)R_0q^2 + \frac{Y_R(q)}{R_0^2}, \tag{18}$$

is renormalized to zero for a certain wave number $q = q^*$, starting from the initial "bare" values $p_R(\Lambda) = p$ (and $Y_R(\Lambda) = Y$, $\kappa_R(\Lambda) = \kappa$) at $q = \Lambda$. Then the correlation function diverges, and the radial deformation mode $\tilde{f}(q^*)$ becomes unstable in the effective harmonic theory with renormalized parameters and initiates the buckling transition. The smallest initial value $p$ for which $D_R(q) = 0$ is reached for some $q = q^*$ is the critical buckling pressure $p_c(T)$. The corresponding unstable wave number $q^*$ replaces the elastic wave number $q_{\rm el} = (Y/\kappa R_0^2)^{1/4} = \pi/l_{\rm el}$ for the $T = 0$ buckling instability, $q^*(T = 0) = q_{\rm el}$. It is important to note that $q^*$ is not identical with the renormalized value $q_{\rm el,R} = (Y_R(q_{\rm el,R})/\kappa_R(q_{\rm el,R})R_0^2)^{1/4}$ of $q_{\rm el}$, because Eq. (19) also contains contributions from the derivatives $\kappa'_R(q)$, $p'_R(q)$, and $Y'_R(q)$ [see also Eq. (A12) in the Appendix].

Because $p_c(T)$ is the smallest initial $p$ for which $D_R(q)$ acquires a zero at $q = q^*$, $D_R(q)$ also has to have a minimum (or saddle) at $q = q^*$. Two cases have to be distinguished: this minimum can be in the interior of the interval of possible q-values, $\pi/R_0 < q^* < \Lambda$, or it can be a boundary minimum at the smallest q-value $q^* = \pi/R_0$.

For an interior minimum or saddle with $\pi/R_0 < q^* < \Lambda$, both $D_R(q^*) = 0$ and $\partial_q D_R(q^*) = 0$ are fulfilled at the critical buckling pressure, which leads to

$$\begin{aligned} 0 = D_R(q) &= \left[\kappa_R(q)q^4 - \frac{1}{2}p_R(q)R_0q^2 + \frac{Y_R(q)}{R_0^2}\right] \\ 0 = \partial_q D_R(q) &= 4\kappa_R(q)q^3 - p_R(q)R_0q \\ &\quad + \left[\kappa_R'(q)q^4 - \frac{1}{2}p_R'(q)R_0q^2 + \frac{Y_R'(q)}{R_0^2}\right]. \end{aligned} \tag{19}$$

These two equations determine both the renormalized critical buckling pressure $p_{c,R} = p_R(q^*)$ and the corresponding unstable wave number $q^*$. If Eqs. (19) lead to a $q^* < \pi/R_0$, the actual minimum is at the boundary value $q^* = \pi/R_0$, and buckling happens at the longest scale, $l^* = \pi/q^* = R_0$. Then, the single equation $D_R(\pi/R_0) = 0$ determines the renormalized critical buckling pressure $p_{c,R} = p_R(\pi/R_0)$. For both cases, the buckling pressure $p_c(T)$ is obtained as the bare initial value $p = p_c(T)$ of the RG transformation which has to be chosen to reach $p_R(q) = p_{c,R}$ at the corresponding buckling wave number $q = q^*$.

In order to determine $p_c(T)$ numerically, instead of solving Eqs. (19), we start at a small bare initial $p$ and follow the RG-flow from $q = \Lambda$ down to the smallest $q = \pi/R_0$. If $D_R(q) = 0$ occurs, buckling happens. The smallest initial $p$ for which this happens is the buckling pressure $p_c(T)$, and the wave number $q$ for which this happens is the unstable wave number $q^*$.

In Ref. [45], a slightly different buckling criterion was employed, namely that there exists a $q = q^*$ where the renormalized external pressure $p_R(q)$ reaches the renormalized critical buckling pressure: $p_R(q^*) = p_{c,R}(q^*) = 4\sqrt{\kappa_R(q^*)Y_R(q^*)}/R_0^2$. This is similar, but not equivalent, to our criterion $D_R(q^*) = 0$ in conjunction with $\partial_q D_R(q^*) = 0$ for a local minimum, because Eq. (19) also contains contributions from $\kappa_R'(q)$, $p_R'(q)$, and $Y_R'(q)$, which are neglected if $p_{c,R}(q^*) = 4\sqrt{\kappa_R(q^*)Y_R(q^*)}/R_0^2$ is used.

The criterion of Ref. [45] can also be interpreted by considering the vertex function $D_R(q^*, q) = \kappa_R(q^*)q^4 - p_R(q^*)R_0q^2/2 + Y_R(q^*)/R_0^2$, which is obtained by integrating out all fluctuations with $\Lambda > q > q^*$, and which governs the remaining long wavelength fluctuations with wave numbers $q$ in $q^* > q > \pi/R_0$. The vertex function $D_R(q^*, q)$ actually has an instability if $p_R(q^*) = p_{c,R}(q^*) = 4\sqrt{\kappa_R(q^*)Y_R(q^*)}/R_0^2$, but the unstable wave number is the renormalized elastic wave number $q_{\mathrm{el,R}} = [Y_R(q^*)/\kappa_R(q^*)R_0^2]^{1/4}$, which differs from $q^*$ in general. If $q_{\mathrm{el,R}} > q^*$, this unstable mode is even no longer accessible to the shell, as it has already been integrated out. As long as differences between $q^*$ and $q_{\mathrm{el,R}}$ are small, the criterion $p_R(q^*) = p_{c,R}(q^*)$ should give comparable results to our criterion $D_R(q^*) = 0$.

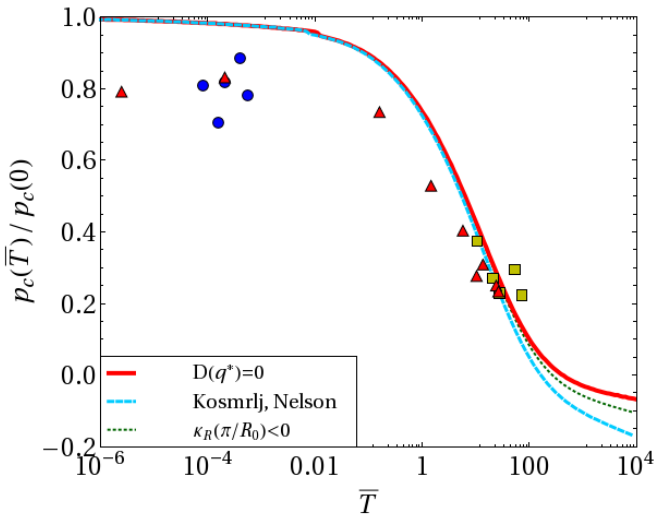


FIG. 3. Critical buckling pressure $p_c(T)$ as a function of the dimensionless temperature $\bar{T} = k_BT\sqrt{\gamma}/\kappa$ according to the buckling criterion $D_R(q^*) = 0$ (dark red solid line) and according to the criterion $p_R(q^*) = p_{c,R}(q^*)$ from Košmrlj and Nelson [45] (light blue dashed line). The criterion $p_R(q^*) = p_{c,R}(q^*)$ gives slightly smaller values of $p_c(T)$ but both criteria lead to $p_c(T) < 0$ for high temperatures signaling that fluctuating shells can spontaneously buckle even without external compressive pressure. We also show the pressure where $\kappa$ first renormalizes to zero at the largest scale, $\kappa_R(\pi/R_0) = 0$ (green dotted line). This pressure is always below the critical $p_c(T)$ from the buckling criterion $D_R(q^*) = 0$ signaling that there are already fluctuations with $\kappa_R < 0$ present before buckling. Data points show numerical results from Ref. [44].

### D. Critical pressure from parameter renormalization

Košmrlj and Nelson have shown that the results of the RG-transformation are solely dependent on a dimensionless temperature

$$\bar{T} \equiv \frac{k_BT\sqrt{\gamma}}{\kappa} \sim \frac{k_BTR_0}{Eh^4} \sim \frac{l_{\mathrm{el}}^2}{l_{\mathrm{th}}^2}. \tag{20}$$

Because our buckling criterion $D_R(q^*) = 0$ operates on renormalized parameters, the critical buckling pressure $p_c(T)$ should also only depend on $\bar{T}$.

Figure 3 shows the critical buckling pressure $p_c(T)$ as a function of the dimensionless temperature $\bar{T}$ for our buckling criterion $D_R(q^*) = 0$ and the criterion $p_R(q^*) = p_{c,R}(q^*)$ used in Ref. [45]. All RG flows have been calculated using an eighth order Runge-Kutta method. First we can confirm that, for both buckling criteria, $p_c(T)$ only depends on the dimensionless temperature $\bar{T}$ for a wide range of Föppl-von Kármán numbers $\gamma \gg 10^3$. This is also corroborated by the scaling collapse of numerical simulation results in Ref. [44] (see also data points in Fig. 3). Only for large $\bar{T}$ results be-

come non-universal, see Fig. 4. This happens if the length scale $l^* = \pi/q^*$ on which buckling occurs according to the criterion $D_R(q^*) = 0$ reaches the largest accessible length scale $R_0$ such that $p_c(T)/p_c(0)$ becomes also $\gamma$-dependent, as can be seen from comparing Fig. 4 and Fig. 5. For small Föppl-von Kármán numbers $\gamma < 10^3$, already the elastic length scale $l_{\rm el}$ on which buckling occurs at $T = 0$ is comparable to the radius $R_0$, and the classical buckling pressure $p_c$ from Eq. (1) is no longer applicable.

For small temperature $\bar{T} < 1$, both criteria give practically identical results. The results are also in rough agreement with the numerical Monte-Carlo simulation results from Ref. [44]. At larger temperatures $\bar{T} \gg 1$, the criterion $p_R(q^*) = p_{c,R}(q^*)$ gives slightly smaller values of $p_c(T)$, i.e., slightly underestimates the buckling stability. Both criteria give rise to $p_c(T) < 0$ for high temperatures, signaling that fluctuating shells can spontaneously buckle even without external compressive pressure [45].

In Fig. 3 we also show the initial pressure for which $\kappa_R(q)$ first renormalizes to zero. This always happens at the largest scale $q = \pi/R_0$ because of the shape of the RG flow of $\kappa_R(q)$: the renormalized $\kappa_R(q)$ is first increasing with $q$ decreasing from its starting value $q = \Lambda$ but, if the renormalized denominator $D_R(q)$ becomes small, exhibits a maximum followed by a sharp decrease to $\kappa_R < 0$. Therefore, negative values $\kappa_R < 0$ are always attained at the largest scales, and $\kappa_R(q) = 0$ is first fulfilled for $q = \pi/R_0$ if starting from small initial pressure. The (blue) line of initial pressures $p$ for which $\kappa_R(\pi/R_0) = 0$ is, except for very small dimensionless temperatures $\bar{T} \lesssim 10^{-4}$, *below* the critical $p_c(T)$ from the buckling criterion $D_R(q^*) = 0$ (red line) in Fig. 3. This shows that there are always unstable bending fluctuations with $\kappa_R < 0$ already present before buckling. These are, however, still stabilized by the last positive term in the vertex function $D_R(q)$ in Eq. (18), which originates from the unavoidable stretching deformation that comes with any bending deformation of a sphere. This effect cannot be captured by the criterion $p_R(q^*) = p_{c,R}(q^*) \propto \sqrt{\kappa_R(q^*)}$ because it will always be fulfilled *before* $\kappa_R = 0$ is reached. Therefore, the (green) line for the initial pressure for which $\kappa_R(q)$ first renormalizes to zero lies *between* the buckling pressures $p_c(T)$ obtained with the two criteria $D_R(q^*) = 0$ and $p_R(q^*) = p_{c,R}(q^*)$ in Fig. 3, and the critical buckling pressures from the criterion $D_R(q^*) = 0$ always lies *above* the critical pressure from the criterion $p_R(q^*) = p_{c,R}(q^*)$.

Figure 5 shows the length scale $l^* = \pi/q^*$ on which buckling occurs according to the criterion $D_R(q^*) = 0$ as a function of the dimensionless temperature $\bar{T}$ and for different Föppl-von Kármán numbers $\gamma$. For large temperatures, the buckling length scale approaches the radius $R_0$, whereas for small temperatures it approaches the classical $T = 0$ elastic length scale $l_{\rm el}$ from Eq. (3). This means that renormalization of elastic constants and pressure effectively transforms buckling into a long wavelength instability at higher temperatures. For small Föppl-von

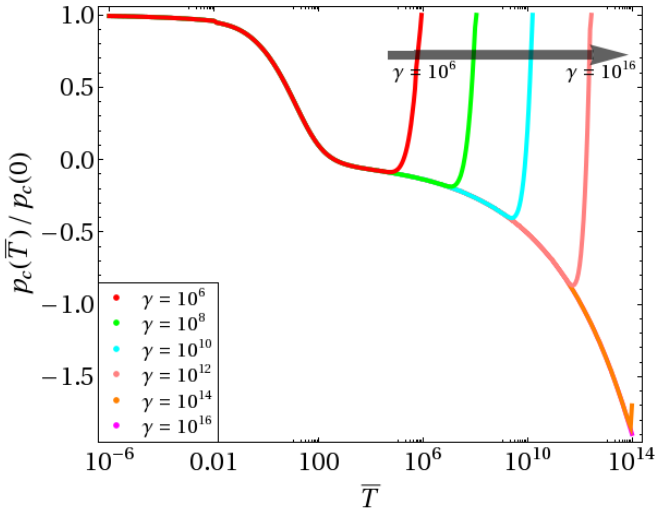


FIG. 4. Non-universality of the critical buckling pressure $p_c(\bar{T})$ for different Föppl-von Kármán numbers $\gamma$ (see arrow). For large values of $\gamma$, the non-universality is shifted to large dimensionless temperatures $\bar{T}$.

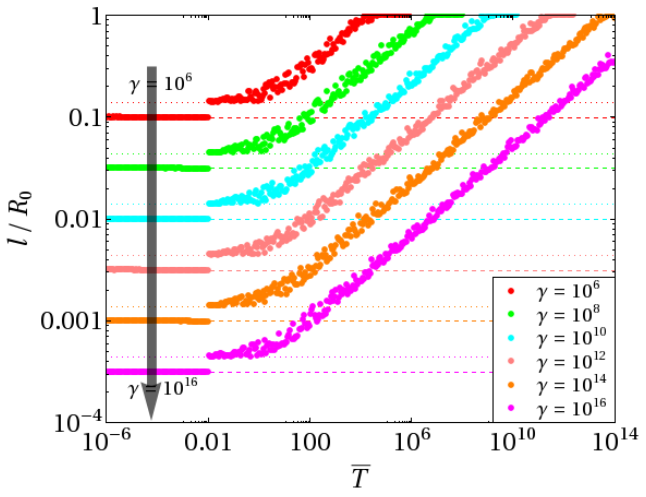


FIG. 5. Length scale $l^*$ on which buckling occurs at the critical buckling pressure as a function of the dimensionless temperature $\bar{T}$ for different Föppl-von Kármán numbers $\gamma$ (see arrow). Dashed lines show the $T = 0$ elastic length scale $l_{\rm el}/R_0$ [Eq. (3)] and dotted lines show $1.4\,l_{\rm el}/R_0$ (see text).

Kármán numbers $\gamma$, the buckling length scale approaches the radius $R_0$ already for smaller dimensionless temperatures $\bar{T}$. If the buckling length $l^*$ approaches $R_0$, results for the critical buckling pressure $p_c(T)$ become non-universal as discussed above (see Fig. 4).

The temperature dependence of the length scale $l^*$ in Fig. 5 shows another remarkable feature for temperatures around $\bar{T} \simeq 0.011$, where it abruptly jumps from values

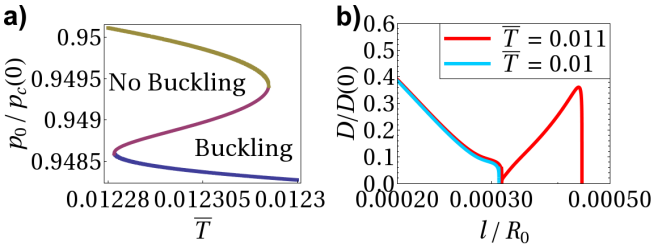


FIG. 6. (a) Critical buckling pressure $p_c(\bar{T})$ in the temperature range $0.01228 < \bar{T} < 0.01233$. (b) $D_R(\ell)$ develops a local minimum as a function of $\ell/R_0$ for temperatures below and above the jump in the buckling length scale ($\bar{T} = 0.01$ (dark red) and $\bar{T} = 0.011$ (light blue), respectively). The jump occurs when the minimum reaches zero, which triggers the buckling criterion $D_R(\ell) = 0$ for $\ell = l^*$.

slightly below the elastic length scale to values about $1.4\,l_{\rm el}$, depicted by the dotted lines. This relation between the length scale before and after the jump is found for a wide range of Föppl-von Kármán numbers $\gamma$. The jump in the buckling length scale can be traced back to the existence of an additional local minimum of $D_R(q)$ for temperatures in the range $0.01 < \bar{T} < 25$. Typically, slightly below the critical pressure $D_R(q)$ has only one local minimum, which develops into a divergence towards negative infinity at $q^*$ if the critical buckling pressure is reached. The jump occurs if two minima are present when the critical buckling pressure is reached and when the global minimum exchanges between both minima right at the buckling pressure [see Fig. 6(b)], meaning that there are two $q^*$-values for which $D_R(q) = 0$. Then the buckling length scale changes discontinuously, whereas the critical buckling pressure remains continuous.

At slightly higher temperatures $\bar{T} \simeq 0.0123$, also the critical buckling pressure exhibits an interesting feature, as it drops abruptly from $p_c(T)/p_c(0) = 0.950$ to $p_c(T)/p_c(0) = 0.949$. In this temperature range an increase in the bare pressure $p$ above the red line in Fig. 6(a) first leads to buckling, i.e., $D_R(q^*) = 0$ is fulfilled for a certain $q^*$. After increasing $p$ above the yellow line, however, we find that again $D_R(q) > 0$ for all $q$. Only above the blue line, a $q^*$ with $D_R(q^*) = 0$ exists again. This leads to an S-shape $p_c(T)$-curve in Fig. 6(a). If the temperature is increased past the end of the blue line in Fig. 6(a), the buckling pressure drops abruptly.

This feature in the $p_c(T)$-curve could be related to the jump in $l^*$ and, thus, to the jump in $q^*$ which we discussed before. This jump happens, however, at slightly lower temperatures. Both the jumps in $l^*$ and in $p_c(T)$ around $\bar{T} \simeq 0.011 - 0.012$ might be artefacts of the approximate RG flow and might disappear if the RG calculation is extended to higher loop order.

## III. BUCKLING BY THERMAL ACTIVATION OVER THE BUCKLING ENERGY BARRIER

Now we address the main issue of the paper, namely buckling by thermal activation over the buckling energy barrier. We use the Pogorelov approach and numerical simulations to determine the energy barrier associated with the formation of a stable axisymmetric dimple for pressures $p < p_c$, i.e., below the critical buckling pressure. If only thermal activation over the energy barrier drives the buckling process, we estimate the critical buckling pressure using the criterion that barriers of order $k_BT$ can be overcome quasi-spontaneously on experimental time scales by thermal activation. Including also renormalization effects of elastic parameters into the energy barrier calculation we describe the combined effect of thermal activation and parameter renormalization. We will also present evidence from numerical simulations that states with multiple dimples are not relevant for the energy barrier and, thus, for thermal activation.

### A. Elastic energies and energy barrier in the Pogorelov model

For the following energetic considerations for indented configurations of spherical shells we will not use the shallow shell approximation but the general form (6) of the stretching energy, the Helfrich form (7) of the bending energy, and the mechanical work $E_p = -p\Delta V$, where $\Delta V$ is the volume reduction with respect to the initial rest state with $V_0 = 4\pi R_0^3/3$. Stretching and bending energy can be brought into dimensionless form by measuring energies in units of $YR_0^2$ and lengths in units of $R_0$. Using also $Y = 4\mu(\mu+\lambda)/(2\mu+\lambda)$ for Young's modulus and $\nu = \lambda/(2\mu+\lambda)$ for Poisson's ratio in the stretching energy, we obtain

$$\begin{aligned}
\frac{E_S}{YR_0^2} &= \frac{1}{2(1+\nu)}\int \frac{\mathrm{d}S}{R_0^2}\left(u_{ik}^2 + \frac{\nu}{1-\nu}u_{ll}^2\right),\\
\frac{E_b}{YR_0^2} &= \frac{2}{\gamma}\int \mathrm{d}S(H-H_0)^2,\\
\frac{E_p}{YR_0^2} &= -\frac{pR_0}{Y}\frac{\Delta V}{R_0^3}.
\end{aligned} \tag{21}$$

We see that the deformation behavior of the sphere only depends on the two parameters $\gamma$ and $\nu$ characterizing the elasticity of the shell and the dimensionless pressure $pR_0/Y$ or, alternatively, $p/p_c$ (because $p_c = 4(Y/R_0)\gamma^{-1/2}$).

Pogorelov approximated the energy of an axisymmetric dimple on a sphere by assuming that the dimple is an approximate isometric deformation of the sphere, i.e., that the dimple is an inverted spherical cap of the undeformed sphere, where the edges of the dimple are rounded by bending energy. Such a mirror inversion of a spherical cap is a suitable starting point to approximate buckled configurations because it avoids additional stretching

strains. Using this approximation, Pogorelov calculated the energy of an axisymmetric indentation of volume $\Delta V$ on a sphere of initial volume $V_0 = 4\pi R_0^3/3$ as [22, 30] [48]

$$U_{\rm Pog}(\Delta V, V_0) = c_{\rm Pog}\frac{YR_0^2}{(1-\nu^2)^{1/4}}\gamma^{-3/4}\left(\frac{\Delta V}{V_0}\right)^{3/4}, \quad (22)$$

where $\nu$ is Poisson's ratio and $c_{\rm Pog} \approx 15.09$, $V_0$ is the initial volume of the sphere, $V < V_0$ its volume after indentation, and $\Delta V = V_0 - V$ the volume reduction by dimple formation. Slightly more accurate estimates of the energy of an axisymmetric dimple are given in [35, 49] but we will use the Pogorelov estimate (22) in the following.

The Pogorelov energy (22) neglects that, under pressure $p$, the spherical shell is already uniformly compressed before the indentation is formed. Uniform compression to a volume $V_0 - \Delta V$ costs an energy

$$U_{\rm sph}(\Delta V) = 4\pi\frac{YR_0^2}{1-\nu}\left[\left(1-\frac{\Delta V}{V_0}\right)^{1/3} - 1\right]^2 \approx \frac{4\pi}{9}\frac{YR_0^2}{1-\nu}\left(\frac{\Delta V}{V_0}\right)^2, \quad (23)$$

where the last approximation holds for $\Delta V \ll V_0$. The equilibrium volume follows from $p = dU_{\rm sph}/d\Delta V$, resulting in

$$p \approx \frac{2}{3}\frac{1}{1-\nu}\frac{Y}{R_0}\frac{\Delta V}{V_0}. \quad (24)$$

During buckling the spherical body relaxes this pre-compression but will remain compressed to a volume $V_0 - \Delta V_b$ (with $\Delta V_b < \Delta V$), in addition to forming an indentation with volume reduction $\Delta V - \Delta V_b$, such that $\Delta V$ is the total volume reduction. The remaining pre-compression of the spherical body costs an energy $U_{\rm sph}(\Delta V_b)$ as given by Eq. (23), the formation of the additional indentation an energy $U_{\rm Pog}(\Delta V - \Delta V_b, V_0 - \Delta V_b)$ as given by Eq. (22). The optimal buckled shape at pressure $p$ is then obtained by minimizing the total enthalpy

$$F(p, \Delta V_b, \Delta V) = U_{\rm sph}(\Delta V_b) + U_{\rm Pog}(\Delta V - \Delta V_b, V_0 - \Delta V_b) - p\Delta V \quad (25)$$

with respect to the spherical pre-compression volume deficit $\Delta V_b$ *and* the total volume deficit $\Delta V$. Under volume control, the total energy $U(\Delta V_b, \Delta V) = U_{\rm sph}(\Delta V_b) + U_{\rm Pog}(\Delta V - \Delta V_b, V_0 - \Delta V_b)$ is minimized with respect to $\Delta V_b$ only, at *fixed* total volume deficit $\Delta V$. We neglect in Eq. (25) the influence of the homogeneous compressional background stress associated with the pre-compression by a volume $\Delta V_b$ on the Pogorelov energy $U_{\rm Pog}$, which is approximately justified as the inverted Pogorelov cap changes stretching strains only at the edges of the indentation. For $\Delta V_b \ll V_0$, we can approximate $U_{\rm Pog}(\Delta V - \Delta V_b, V_0 - \Delta V_b) \approx U_{\rm Pog}(\Delta V - \Delta V_b, V_0)$.

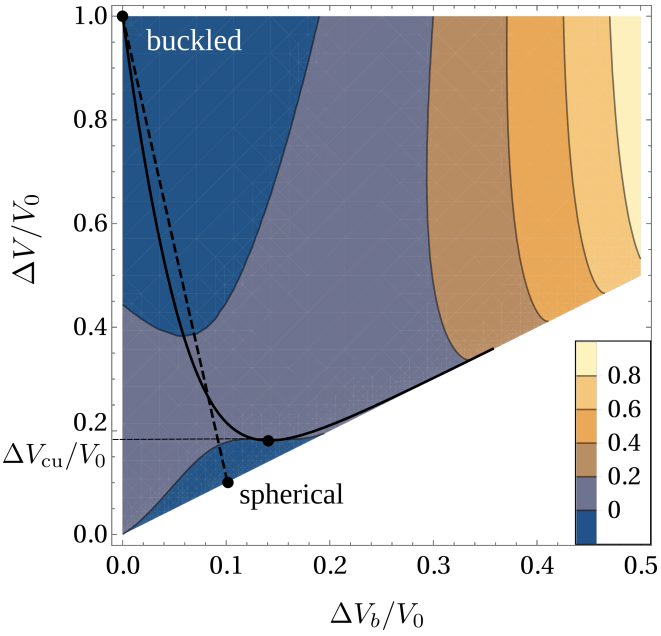


FIG. 7. Contour plot of Pogorelov enthalpy $F(p, \Delta V_b, \Delta V)/YR_0^2$ as a function of pre-compression volume $\Delta V_b$ of the spherical capsule body and total volume deficit $\Delta V$ with $\Delta V_b \le \Delta V$ ($\gamma = 100$, $pR_0/Y = 0.15 > p_{c1}$, $\nu = 1/2$, $F$ in units of $YR_0^2$). Solid black lines represent local minima and maxima as a function of $\Delta V_b$, which only exist above the critical unbuckling volume deficit $\Delta V_{\rm cu}$. Along the dashed path from the metastable spherical shape to the buckled shape, the energy barrier $F_{\rm B}$ from Eq. (29) has to be overcome.

Then, equilibrium states under volume control become equivalent to equilibrium states under pressure control with an effective pressure $p = dU_{\rm sph}(\Delta V_b)/d\Delta V_b$ generated by the compressional stress of the spherical body.

Analyzing the $\Delta V_b$-dependence of $U(\Delta V_b, \Delta V)$ for fixed $\Delta V$ shows that the compressed spherical shape with $\Delta V_b = \Delta V$ remains a metastable minimum for *all* $\Delta V$ (see Fig. 7). This is an artefact of the Pogorelov approximation, which is not able to predict the classical buckling pressure $p_c$ or the critical classical buckling volume given by [29]

$$\frac{\Delta V_c}{V_0} = 1 - \left[\frac{1}{2} + \sqrt{\frac{1}{4} + 2(1-\nu)\gamma^{-1/2}}\right]^{-3} \approx 6(1-\nu)\gamma^{-1/2} \quad (26)$$

(the last approximation applies to $\gamma \gg 1$). This is the volume where the compressive pressure in a sphere reaches the classical buckling pressure $p_c = 4(Y/R_0)\gamma^{-1/2}$ [see Eq. (1)] according to the pressure-volume relation (24) in the compressed spherical shape.

Under volume control, the total energy $U(\Delta V_b, \Delta V)$ can develop a second local minimum as a function of $\Delta V_b$, which corresponds to a buckled state (see Fig. 7). This

minimum with respect to $\Delta V_b$ only exists for sufficiently large total volume reduction

$$\frac{\Delta V}{V_0} \geq \frac{\Delta V_{\rm cu}}{V_0} = \frac{5}{4^{4/5}}\left(\frac{27c_{\rm Pog}}{32\pi}\right)^{4/5}\frac{(1-\nu)^{4/5}}{(1-\nu^2)^{1/5}}\gamma^{-3/5} = 5.05\frac{(1-\nu)^{4/5}}{(1-\nu^2)^{1/5}}\gamma^{-3/5}, \quad (27)$$

and we obtain a *critical unbuckling volume deficit* $\Delta V_{\rm cu}$ below which the buckled state has to spontaneously "unbuckle". This lower critical volume deficit also corresponds to the minimum volume on the pressure-volume relation of the buckled branch and has also been found in Ref. [35]. The critical unbuckling volume deficit shows a different power-law dependence $\Delta V_{\rm cu} \propto \gamma^{-3/5}$ on the Föppl-von Kármán number as compared to the classical buckling volume $\Delta V_c \propto \gamma^{-1/2}$ in Eq. (26). For $\Delta V > \Delta V_{\rm cu}$, minimization with respect to $\Delta V_b$ gives the optimal pre-compression

$$\frac{\Delta V_b}{V_0} \approx \frac{27c_{\rm Pog}}{32\pi}\frac{1-\nu}{(1-\nu^2)^{1/4}}\gamma^{-3/4}\left(\frac{\Delta V}{V_0}\right)^{-1/4} \quad (28)$$

in the buckled state (for $\Delta V_b \ll \Delta V$).

Under pressure control, the buckled state becomes a local minimum of the enthalpy $F(p, \Delta V_b, \Delta V)$ as a function of both $\Delta V_b$ and $\Delta V$ only for sufficiently large pressure $p > p_{\rm cu}$, i.e., above a *lower critical unbuckling pressure*, which is given by the condition that the maximally buckled state $\Delta V = V_0$ ($\Delta V_b = 0$) becomes metastable: $p_{\rm cu} = \partial U_{\rm Pog}/\partial \Delta V(V_0, V_0)$. We find $p_{\rm cu} \propto (Y/R_0)\gamma^{-3/4}$, again with a different parameter dependence as compared to the classical buckling pressure $p_c \propto (Y/R_0)\gamma^{-1/2}$ [see Eq. (1)]. The maximally buckled state becomes energetically favorable over the spherical state for $p > p_{c1}$, i.e., above the Maxwell pressure $p_{c1} = 4p_{\rm cu}/3 \propto (Y/R_0)\gamma^{-3/4}$ [29, 30].

In the modified Pogorelov enthalpy landscape $F(p, \Delta V_b, \Delta V)$ (see Fig. 7), the metastable spherical state $\Delta V_b = \Delta V$, which exists for $p > p_{\rm cu}$, is always protected by an energy barrier from spontaneous transitions into the buckled state. This energy barrier can be determined from starting at a spherical initial state $\Delta V_b = \Delta V = \Delta V_i$ and moving along a path $(\Delta V_b, \Delta V) = (\Delta V_i, \Delta V_i) + v(-A, 1)$ in the $\Delta V_b$-$\Delta V$-plane into an arbitrary direction $(-A, 1)$ with decreasing $\Delta V_b$ ($A > 0$) using a volume parameter $v \geq 0$. Independently of $A$ we find an energy barrier

$$F_{\rm B}(p) = a(\nu)YR_0^2\gamma^{-3/2}\left(\frac{p}{p_c}\right)^{-3} = \tilde{a}(\nu)\frac{Eh^4}{R_0}\left(\frac{p}{p_c}\right)^{-3} \quad (29)$$

with

$$a(\nu) \equiv \frac{27^2}{\pi^3 2^{20}}c_{\rm Pog}^4\frac{1}{1-\nu^2} \simeq \frac{1.16}{1-\nu^2},$$

which is assumed at a total indentation volume $(\Delta V - \Delta V_b)/V_0 = (1+A)v/V_0 \sim \gamma^{-1}(p/p_c)^{-4}$. This result is only valid for $p/p_c \gg \gamma^{-1/4}$ (or $p \gg p_{\rm cu}$) such that $(\Delta V - \Delta V_b)/V_0 \sim \gamma^{-1}(p/p_c)^{-4} \ll 1$ and dimples remain small compared to the total capsule volume. The transition state, where this maximum is assumed, is a sphere with an energetically unfavorable "flattened" dimple, which is unstable both with respect to shrinking back to a sphere and growing into a fully developed dimple. For a fixed mechanical pressure, the fully developed dimple actually snaps through until opposite sides are in contact. Only for a volume-dependent osmotic pressure or under strict volume control, a stable dimple of finite size is possible [29, 30]. The buckling shapes that are assumed around the barrier if also multiple dimples are allowed are discussed below in Sec. III D. The result (29) describes the energy barrier for a single axisymmetric dimple.

It is clear that the Pogorelov model is incorrect for very large and very small dimples as the assumption that the dimple can be described as a rounded mirror inversion fails in both of these limits. For very small dimples this can be easily seen by the fact that the energy barrier (29) does not disappear for $p \geq p_c$. We can, however, assume that very shallow dimples of a depth $\zeta$ comparable to the layer thickness $h$ (assuming a thin shell made from an isotropic elastic material), i.e., $\zeta \sim h$, can be formed spontaneously (a similar assumption is made in Ref. [13] to derive the classical buckling pressure $p_c$). Using the fact that the dimple opening angle is $\alpha \sim \sqrt{\zeta/R_0}$ and $\Delta V \sim \alpha^4 R_0^3 \sim \zeta^2 R_0$ such a small dimple of volume $\Delta V/V_0 \sim h^2/R_0^2 \sim \gamma^{-1}$ costs an energy $U_{\rm Pog}/YR_0^2 \sim \gamma^{-3/4}(h/R_0)^{3/2} \sim \gamma^{-3/2}$ according to Eq. (22). Comparing with the barrier scaling (29) we conclude that exactly at $p \sim p_c$ the energy barrier reduces to this energy and could, thus, be overcome spontaneously. The Pogorelov result (29) for the energy barrier is only a good approximation for $p \ll p_c$ (in practice, $p < 0.8\,p_c$, see Fig. 20 in the Appendix) such that dimples are large enough, but $p/p_c \gg \gamma^{-1/4}$ (or $p \gg p_{\rm cu}$) such that $\Delta V/V_0 \sim \gamma^{-1}(p/p_c)^{-4} \ll 1$ and dimples remain small compared to the total capsule volume. If $p$ approaches $p_c$ the buckling energy barrier actually vanishes as our simulation results in the next section show.

### B. Simulation results for the energy barrier

In order to investigate the behavior of the energy barrier for single axisymmetric dimples also for $p \leq p_c$, i.e., for small dimples more rigorously, we use numerical energy minimization with the Surface Evolver [50]. Some details are explained in Appendix B.

Recently, a number of publications addressed the energy barrier for axisymmetric dimples on spherical shells by applying an additional point force in order to induce formation of a single dimple, where the point force $F$ is applied, and in order to control the indentation depth $\zeta$ by the point force [34, 35, 40, 41]. The barrier state corresponds to an indented state with $F = 0$ at $\zeta = \zeta_B$, which is unstable with respect to growth and shrinkage.

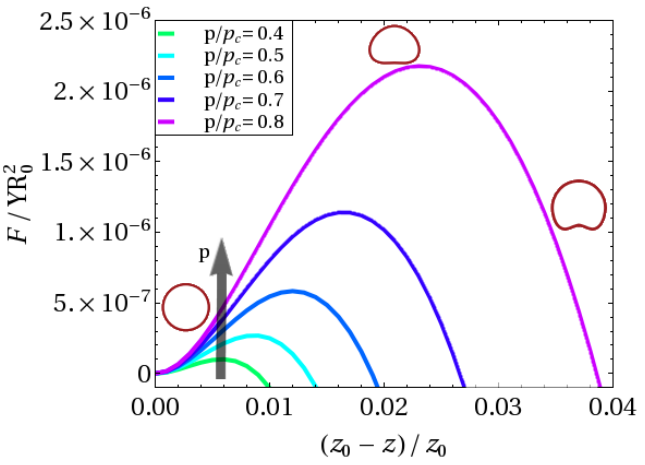


FIG. 8. Numerical results for the enthalpy as a function of the dimensionless indentation depth $(z-z_0)/z_0 = 2\zeta/R(p)$ for $\gamma = 10^5$, $\nu = 0.3$, and for different values of $p/p_c$ (choosing $F(z = z_0) = 0$ for an initial vertex distance $z_0 = 2R(p)$). The buckling energy barrier is obtained from the enthalpy maximum. Representative schematic shapes are shown for the spherical initial state, the barrier state with a "flattened" dimple, and a buckled state with a well-developed dimple (note that, under pressure control, the fully developed dimple corresponding to the buckled energy minimum will snap through until opposite sides are in contact). The indentations in the schematic shapes are exaggerated; the actual dimple indentations are much smaller, c.f. values on the $x$-axis.

The energy barrier is obtained from the $F(\zeta)$-relation by $U_B = \int_0^{\zeta_B} F(\zeta)d\zeta$. An additional point force has also been used in experiments [39] in order to calculate the energy barrier. In our numerical approach we will not prescribe a point force but directly constrain the conjugated indentation depth $\zeta$.

In the simulation, we construct a spherical rest shape and apply a pressure $p < p_c$, which leads to a uniformly compressed sphere with radius $R(p) < R_0$. In order to map out the energy barrier between the compressed spherical state and the final buckled state, we need to stabilize all intermediate transition states in the numerical simulation. This is done by selecting two points on opposite sides of the sphere and introducing an additional constraint on the distance $z$ between these two points during energy minimization (corresponding to an indentation depth $\zeta = R - z/2$). Constraining and decreasing the distance $z$ between these two points allows us to control the size of the two dimples that are formed on opposite sides of the sphere. For sufficiently small dimples, the enthalpy of a single dimple is half of the enthalpy of two dimples [40], as we numerically verify in Fig. 18 in Appendix B). This allows us to obtain the enthalpy landscape $F = F(z)$ of a single dimple as a function of $z$ for a given pressure $p$ (see Fig. 8), from the maximum of which we can directly determine the energy barrier $F_B$.

As has been shown above, energies of deformed shells only depend on two parameters $\gamma$ and $\nu$ characterizing the elasticity and the dimensionless pressure $p/p_c$. This also applies to the energy barrier, which, if measured in units of $YR_0^2$, should only depend on these parameters. To analyze simulation results we use the critical pressure $p_{c,SE}$ as obtained from Surface Evolver simulations rather than the theoretical value $p_c = 4(Y/R_0)\gamma^{-1/2}$ from Eq. (1) in order to compensate for discretization effects from triangulation of the surface, as explained in Appendix B 1. The Pogorelov approximation (29) suggests that the energy barrier can be written as a product

$$\frac{F_B(p)}{YR_0^2} = f_\nu(\nu)\gamma^{-\alpha} f_p\left(\frac{p}{p_c}\right), \tag{30}$$

with a function $f_\nu(\nu)$, an exponent $\alpha$, and a scaling function $f_p(x)$ for the pressure-dependence, which has to be determined from the numerical simulation results. Our numerical results for the energy barrier as a function of $p/p_{c,SE}$ for several values of $\gamma$ and $\nu$ are shown in Fig. 9. Figure 9(a) demonstrates that, for $\nu \leq 0.5$, the $\nu$-dependence is very weak as in the Pogorelov approximation [where $f_\nu(\nu) = a(\nu)$, cf. Eq. (29)] such that we simply choose $f_\nu(\nu) \approx 1$ for $\nu \leq 0.5$. Figure 9(c) shows that data for different $\gamma$ (Fig. 9(b)) almost perfectly collapse for an exponent

$$\alpha = 1.52 \approx 3/2, \tag{31}$$

which is also in agreement with the Pogorelov approximation. As a result we can read off the scaling function $f_p(x)$ from Fig. 9(c), which shows clear deviations from the Pogorelov approximation $f_p(x) \sim x^{-3}$ for larger $x \leq 1$. For small $x$ we find $f_p(x) \sim x^{-2.8}$ close to the Pogorelov approximation. A numerical approximation $f_{p,num}(x)$ for the scaling function is given in Appendix B 2 in Eq. (B3). Numerically, we see that the energy barrier vanishes upon approaching the critical pressure $p_c$, as opposed to the Pogorelov energy barrier (29). Our data is fairly well described by $F_B(p) \propto (1 - p/p_c)^2$ for $p \approx p_c$ (or $f_{p,num}(x) \propto (1-x)^2$ for $x \approx 1$).

Our numerical results are in excellent agreement with experimental data from Ref. [39], where the energy barrier has been determined from experiments on hemispherical shells subject to both compressive pressure and a probing point force controling depth of the indentation. A comparison with the rescaled experimental data from Ref. [39] is also shown in Fig. 9(c).

In order to determine the $\nu$-dependence more exactly, i.e., to obtain a more accurate approximation for the function $f_\nu(\nu) \approx 1$ in Eq. (30), we perform simulations for different values of $\gamma$ and different values of $\nu$, and isolate $f_\nu(\nu)$ by plotting the rescaled energy barrier

$$\frac{F_B(p)\gamma^{1.52}}{YR_0^2 f_{p,num}(p/p_{c,SE})} = f_\nu(\nu) \tag{32}$$

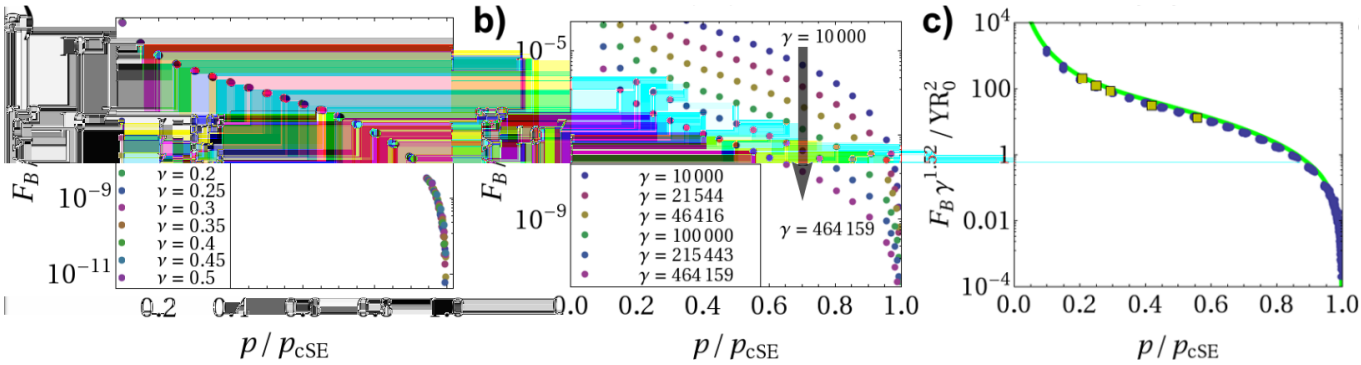


FIG. 9. Energy barrier as a function of the pressure for (a) several values of $\nu$ at $\gamma = 10^5$ and (b) several values of $\gamma$ (see arrow) at $\nu = 0.3$. (c) Collapse of the energy barrier for different values of $\gamma$ (dots). The numerical approximation $f_{\mathrm{p,num}}(p/p_{\mathrm{c,SE}})$ for the scaling function from Eq. (B3) is shown as green line. For small pressures, the energy barrier scales as $p^{-2.8}$, which is close to the $p^{-3}$-law from the Pogorelov approximation (29). In the collapse we also inserted the experimental data from Ref. [39] (yellow squares) which shows excellent agreement with our numerical results.

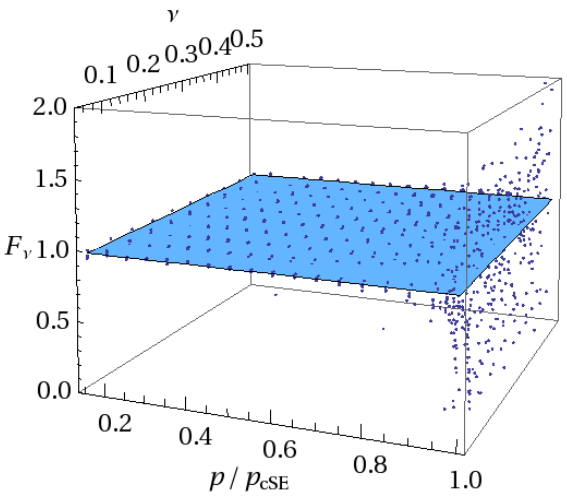


FIG. 10. Energy barrier rescaled according to Eq. (32) as a function of $\nu$ and $p/p_{\mathrm{c,SE}}$ for $\nu \leq 0.5$ (dots). Additionally, a linear fit $f_\nu(\nu) = \mathrm{const} + 0.086\nu$ is shown (plane). The values for very large pressures scatter because of the numerical errors in the determination of the critical pressure $p_{\mathrm{c,SE}}$ and because the determination of energy barriers for large pressures or small dimples becomes less exact, as small changes to the sphere can cause buckling in this regime. Therefore, only values $p/p_{\mathrm{c,SE}} < 0.8$ are used for fitting $f_\nu(\nu)$.

in Fig. 10, where we use the scaling function $f_{\mathrm{p,num}}(x)$ from Fig. 9(c). For $\nu \leq 0.5$, a linear fit $f_\nu(\nu) = 0.98 + 0.086\nu$ describes the data [see also Eq. (B4)].

Using the numerically determined functions $f_{\mathrm{p,num}}(x)$ and $f_\nu(\nu)$ we obtain an accurate description of the numerical results, which is summarized in the Appendix B 2 in Eq. (B1). A simple approximation formula, which is accurate to within 20%, is obtained using $f_\nu(\nu) \approx 1$, $\alpha = 3/2$, and

$$\frac{F_{\mathrm{B}}(p)}{Y R_0^2} \simeq \gamma^{-3/2} f_{\mathrm{p,app}}\left(\frac{p}{p_c}\right)$$
$$f_{\mathrm{p,app}}(x) = 1.44\,(1-x)^2(x^{-3} + 34.1\,x^{-1}). \qquad (33)$$

The approximative scaling function $f_{\mathrm{p,app}}(x)$ is motivated by the Pogorelov result $F_{\mathrm{B}}(p) \propto p^{-3}$ for small $p \ll p_c$ and our numerical result $F_{\mathrm{B}}(p) \propto (1 - p/p_c)^2$ for $p \approx p_c$. The $x^{-1}$-term represents a $p^{-1}$-correction to the Pogorelov result.

### C. Critical pressure from thermal activation

Our results for the energy barrier can be used to estimate a time scale on which buckling will occur by thermal activation. According to Kramers theory, i.e., assuming effectively overdamped stochastic dynamics for a reaction coordinate characterizing the size of the dimple such as $z$ or $\Delta V$, this time scale is

$$t_B = \tau e^{F_{\mathrm{B}}(p)/k_B T}, \qquad (34)$$

where $\tau_0$ is a microscopic time scale characterizing the dynamics of the reaction coordinate and where the Arrhenius factor $\exp(F_{\mathrm{B}}/k_B T)$ dominates. For a given experimentally accessible time scale $t_{\mathrm{exp}}$ buckling occurs if

$$F_{\mathrm{B}}(p) < k_B T \ln(t_{\mathrm{exp}}/\tau) \sim k_B T, \qquad (35)$$

which is essentially the criterion that energy barriers $F_{\mathrm{B}}(p) < k_B T$ can be overcome by thermal activation quasi-spontaneously (as long as they are not several orders of magnitude between time scales $t_{\mathrm{exp}}$ and $\tau$). The criterion $F_{\mathrm{B}}(p_c(T)) = k_B T$ then determines an effective temperature-dependent buckling pressure $p_c(T)$ for buckling by thermal activation.

First, we use this criterion with our $T = 0$ results for the buckling energy barrier from the previous section. Employing the Pogorelov approximation (29) we obtain

$$\frac{p_c(T)}{p_c} = a^{1/3}(\nu)\left(\frac{k_BT}{\kappa}\gamma^{1/2}\right)^{-1/3} = a^{1/3}(\nu)\bar{T}^{-1/3} \quad (36)$$

for $\bar{T} \gg 1$ such that $p_c(T) \ll p_c$. This result is only valid where the Pogorelov approximation is valid, i.e., for $0.8 > p_c(T)/p_c \gg \gamma^{-1/4}$ as discussed above, which means $0.8^{-3} < \bar{T} \ll \gamma^{3/4}$ in Eq. (36).

Using the numerical results for the energy barrier in the scaling form $F_B(p)/YR_0^2 \approx f_\nu(\nu)\gamma^{-3/2} f_{p,num}(x)\,(p/p_c)$ with the scaling function $f_{p,num}(x)$ given by the collapse in Fig. 9(c), we obtain the buckling criterion

$$f_{p,num}\left(\frac{p_c(T)}{p_c}\right) = \frac{1}{f_\nu(\nu)}\frac{k_BT}{\kappa}\gamma^{1/2} = \frac{\bar{T}}{f_\nu(\nu)} \quad (37)$$

for buckling by thermal activation. The resulting critical buckling pressure $p_c(T)$ is shown in Fig. 11 (dark red line) and lies slightly above the critical buckling pressure from parameter renormalization. In the absence of thermal fluctuations, the r.h.s. vanishes and Eq. (37) reduces to the correct result $p_c(0)/p_c = 1$ because this is the pressure where also the barrier function $f_{p,num}\,(p_c(0)/p_c)$ on the l.h.s. vanishes. With $f_\nu(\nu) \approx 1$ and $f_{p,num}(x) \approx 1.44\,(1-x)^2$ [see Eq. (33)] we can also infer the crossover to the $T = 0$ result: $p_c(T)/p_c \approx 1 - (\bar{T}/1.44)^{1/2}$. Interestingly, also the criterion (37) for buckling by thermal activation only depends on the dimensionless temperature $\bar{T}$ as also observed for the influence of parameter renormalization on the buckling instability, see Fig. 3.

So far, we did not take the combined effects of *both* thermal activation *and* renormalization of the parameters $\kappa$, $Y$, and $p$ by anharmonicities into account in the buckling criteria. This can be done by using properly renormalized parameters $\kappa_R$, $Y_R$, and $p_R$ in the barrier crossing criterion $F_B(p) = k_BT$, which leads to

$$f_{p,num}\left(\frac{p_R(q^*)}{p_{c,R}(q^*)}\right) = \frac{\bar{T}}{f_\nu(\nu)}, \quad (38)$$

where $p_R(q^*)$ is the renormalized pressure and $p_{c,R}(q^*) = 4\sqrt{\kappa_R(q^*)Y_R(q^*)}/R_0^2$ the renormalized critical buckling pressure. The renormalization of $\nu$ need not be considered, because of the negligible effect of $\nu$ on the energy barrier, and because $\nu$ remains of order unity during the renormalization [51]. The critical buckling pressure $p_c(T)$ in the presence of thermal activation is the smallest initial pressure for which criterion (38) can be fulfilled.

The question remains to be answered how to choose the length scale $l^* = \pi/q^*$ in Eq. (38) up to which barrier parameters are renormalized in the modified criterion $F_{B,R}(q^*)/k_BT = 1$. The transition state at the energy maximum is a sphere with an energetically unfavorable "flattened" dimple (see also Fig. 8) and the elastic parameters characterizing this transition state dimple can only be renormalized by fluctuations on length scales smaller than the size of the dimple. At finite temperatures, the minimal transition state dimple size is set by the unstable wave number $q^*$ for buckling, which we determined by our above buckling criterion $D_R(q^*) = 0$ or the approximative buckling criterion $p_R(q^*) = p_{c,R}(q^*)$ from Ref. [45] from parameter renormalization. At $T = 0$, the buckling length scale $l^*$ approaches the elastic length scale $l_{el} \sim R_0\gamma^{-1/4}$ for the unstable wave length at the $T = 0$ buckling instability (see Fig. 5). At $p = p_c$ and $T = 0$, the elastic length scale $l_{el}$ also sets the size of the transition state dimple. For $p_c > p > p_{c1}$, the $T = 0$ transition state dimple size can be obtained from the enthalpy landscape $F(p, \Delta V_b, \Delta V)$, for which we showed above that the barrier state is assumed for an indentation volume $(\Delta V - \Delta V_b)/V_0 \sim \gamma^{-1}(p/p_c)^{-4}$. Assuming a spherical cap shaped dimple, this corresponds to a transition state dimple size $\sim R_0\gamma^{-1/4}p_c/p$, which increases with decreasing pressure. It reaches its maximally possible size $R_0$ at the Maxwell pressure $p_{c1}$ above which buckling becomes energetically possible and reduces to $l_{el} \sim R_0\gamma^{-1/4}$ at $p = p_c$. Therefore, also at finite temperatures, we expect the transition state dimple size to be somewhat larger than $l^*$ for $p < p_c(T)$. At $T = 0$, the length scale $l_{el}$ remains the length scale of the width of the ridge of the Pogorelov dimple [32, 33] also for $p < p_c$. In analogy

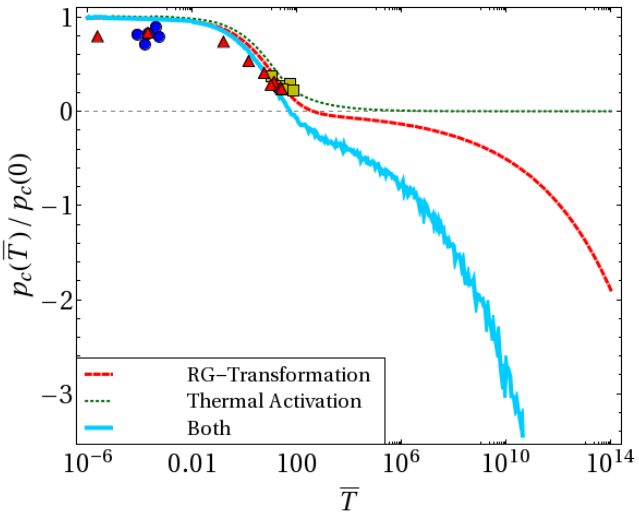


FIG. 11. Critical buckling pressure $p_c(T)$ as a function of the dimensionless temperature $\bar{T} = k_BT\sqrt{\gamma}/\kappa$ according to the buckling criterion $D_R(q^*) = 0$ which includes renormalization effects only (dark red dashed line, see also red solid line in Fig. 3), $p_c(T)$ according to the criterion $F_B(p_c(T)) = k_BT$ or Eq. (37) for thermal activation over the buckling energy barrier (green dotted line, for $\nu = 1/3$), and $p_c(T)$ according to the generalized criterion $F_{B,R}(q^*)/k_BT = 1$ or Eq. (38) which combines renormalization effects and thermal activation (light blue solid line, for $\nu = 1/3$). Inclusion of thermal activation leads to a decrease of the critical buckling pressure for $\bar{T} > 1$. As in Fig. 3, data points show numerical results from Ref. [44].

with the $T = 0$ case, we expect that the length scale $l^*$ determined by our above buckling criterion $D_R(q^*) = 0$ corresponds to the width of the Pogorelov dimple ridge in the presence of thermal fluctuations rather than the size of the dimple. Thus, in choosing $q^*$ from the buckling criterion $D_R(q^*) = 0$ in Eq. (38), we use parameters, which are renormalized only up to the length scale of the ridge of the dimple.

In using renormalized parameters in the buckling criterion (38), which includes thermal activation, we also assumed that the same RG equations (15) that are derived for fluctuation around a spherical background state can still be applied to describe fluctuations around the transition state which already contains the "flattened" dimple. The RG equations will most likely take a different form on length scales exceeding the Pogorelov ridge scale $l^*$ because stretching and bending strains with this wavelength are large in a dimple configuration. Stretching and bending modes with smaller wave lengths should remain small and unaffected by the dimple such that they are well described by the RG equations (15) for a spherical background.

If the length scale $q^*$ is chosen from the approximative buckling criterion $p_R(q^*)/p_{c,R}(q^*) = 1$ from Ref. [45], Eq. (38) can be written as $p_R(q^*)/p_{c,R}(q^*) = f^{-1}_{\mathrm{p,num}}[\bar{T}/f_\nu(\nu)]$ (with $f^{-1}_{\mathrm{p,num}}$ as inverse function of $f_{\mathrm{p,num}}$) and viewed as direct generalization of this criterion in the presence of thermal activation. The combined effect of thermal activation and parameter renormalization then leads to a further reduction of the critical buckling pressure, in particular, for temperatures $\bar{T} > 1$. This is what we expect in general: if both buckling mechanisms are considered, the critical buckling pressure should be further lowered below our above results in Fig. 3 from parameter renormalization only.

If the length scale $q^*$ is chosen from our buckling criterion $D_R(q^*) = 0$, we obtain the generalized critical pressures $p_c(T)$ in Fig. 11 (blue solid line). Again, the combined effect of thermal activation and parameter renormalization leads to a further reduction of the critical buckling pressure for temperatures $\bar{T} > 1$. The available numerical Monte-Carlo simulation results from Ref. [44], which are also shown in Fig. 11, do not lie in the temperature range $\bar{T} \gg 1$, where the additional reduction becomes most pronounced demonstrating the need for further simulations in this temperature range.

### D. Buckling shapes

So far only spheres with one or two dimples have been considered. However, as the mode that becomes unstable for $p \geq p_c$ produces multiple dimples, and, in fact, the initial buckling shapes are a combination of critical modes [25, 26], as shown in Fig. 12, such shapes must also be taken into account. The question remains to what extent configurations with multiple dimples represent also relevant intermediate states for the energy barrier for $p < p_c$,

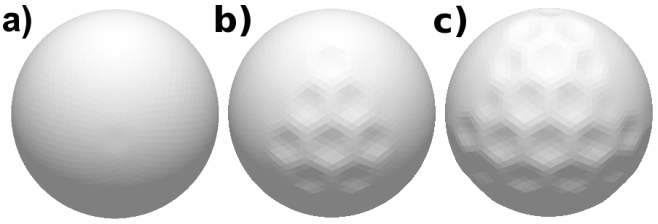


FIG. 12. Postbuckling shapes obtained from numerical energy minimization with a constrained variance $\Delta R^2$ and unconstrained $z$ for (a) $\Delta R^2/R_0^2 = 1.3 \cdot 10^{-7}$, (b) $\Delta R^2/R_0^2 = 1.5 \cdot 10^{-5}$, and (c) $\Delta R^2/R_0^2 = 4.7 \cdot 10^{-5}$ for $p/p_c = 0.85$.

i.e., whether they represent the optimal transition states between the metastable compressed spherical state and the buckled state. The final buckled state will have only a single dimple.

In order to compare enthalpies of states with single dimples and states with multiple dimples, we use two types of constraints. The first type is a constraint on the variance $\Delta R^2$ of the distance of every vertex on the sphere to its center (the center of the sphere is considered to be the average of the coordinates of all vertices). The variance $\Delta R^2$ of a spherical state before buckling is zero, whereas $\Delta R^2 > 0$ after buckling, both for a single dimple and multiple dimples (see Fig. 12). By constraining the variance, we stabilize buckling shapes both with single and multiple dimples. The second type of constraint is similar to the constraint on the distance $z$ between two opposite vertices on the sphere, which we used in Sec. III B. Now, we fix, however, the position of one vertex and constrain the other vertex to a distance $z$. For a constrained $z < 2R_0$ a single dimple of depth $\zeta = 2R_0 - z$ will be formed. We apply both constraints to the buckled shapes and compare the enthalpy $F$ for different target values for $\Delta R^2$. If the minimal enthalpy for a given target value of $\Delta R^2$ without an additional $z$-constraint can also be reached in the presence of a $z$-constraint, we can conclude that this enthalpy minimum represents a configuration with a single dimple. If, on the other hand, the minimal enthalpy for a given target value of $\Delta R^2$ without an additional $z$-constraint cannot be reached in the presence of a $z$-constraint, we conclude that this enthalpy minimum is a configuration with multiple dimples.

The results for the enthalpy minima as a function of $\Delta R^2$ are shown in Fig. 13. The black line is the minimal enthalpy without additional $z$-constraint, and the colored lines are enthalpy minima in the presence of both constraints with color-coded $z$-value. The black line or the envelops of the colored lines exhibit a maximum which is the enthalpy barrier for buckling. If the colored lines remain above the black line for unconstrained $z$, the optimal buckled configuration consists of an array of multiple dimples. If the colored lines of the $z$-constrained enthalpy touch the black line for unconstrained $z$ (i.e., the black line is the envelope of the colored lines), we conclude that the optimal buckled configuration consists

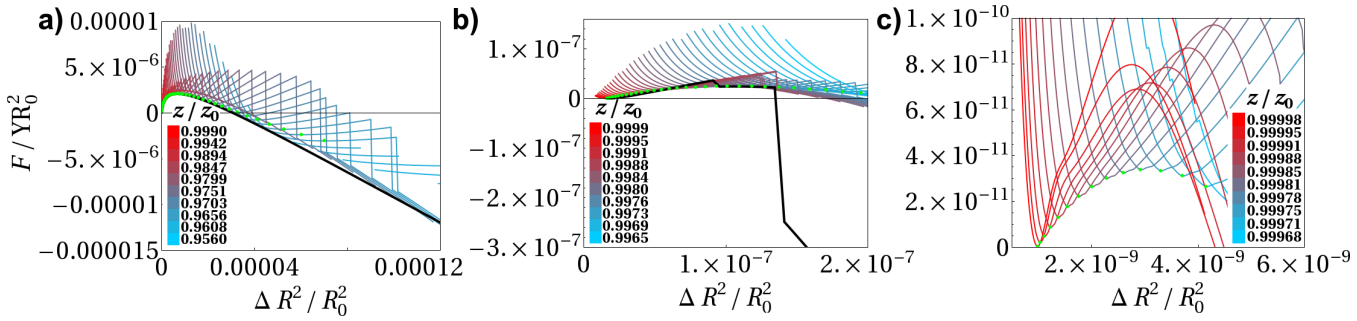


FIG. 13. Minimal enthalpy as a function of $\Delta R^2$ obtained by the two outlined approaches, i.e., for constrained $z$ (colored lines) or unconstrained $z$ (thick black lines) for $\gamma = 100000$, $\nu = 0.3$, and $p/p_c = 0.3$ (a), $p/p_c = 0.85$ (b), and $p/p_{c,\mathrm{SE}} \approx 0.998$ (c). Lines of different colors correspond to different values of $z$. Green dots show local energy minima for different values of $z/z_0$ with $z_0$ being the initial value of $z$, before deformation. (a) The colored lines of the $z$-constrained enthalpy touch the black line for unconstrained $z$ (i.e., the black line is the envelope of the colored lines) indicating that the optimal buckled configuration consists of a single dimple. (b) Jumps in the colored and black curves are caused by large inward moves of a vertex in the center of the indentation when the indentation switches from its initial concave into its final convex shape. These jumps occur behind the initial energy barrier. The black line shows small deviations from the envelope of the colored lines for small $\Delta R^2$ because the location of a single dimple is determined by the $z$-constraint (colored lines), whereas the initial formation and location of dimples is strongly influenced by the presence of disclinations for unconstrained $z$ (black line). (c) Close to the critical pressure the influence of the disclinations is even stronger (therefore, data for unconstrained $z$ is not shown).

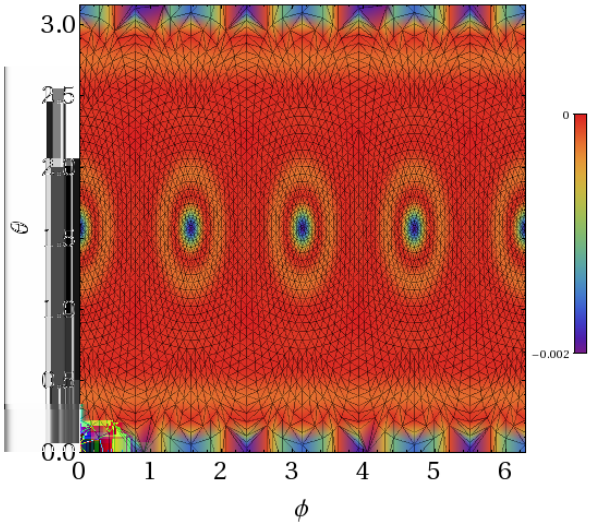


FIG. 14. $R(\phi,\theta) - \bar{R}$, in spherical coordinates, where $R(\phi,\theta)$ is the distance to the center of the sphere, and $\bar{R}$ is its average, for an additional $z$-constraint and directly before the first jump in Fig. 13(b) for $p/p_c = 0.85$. The variance $\Delta R^2$ is mostly caused by six four-fold disclinations (4 at $\theta \sim \pi/2$ and one at $\theta = 0, \pi$), such that the triangulation determines the formation and location of six dimples instead of a single dimple. As a result the black line in Fig. 13(b) does not envelope the colored lines in Fig. 13(b) for small $\Delta R^2$.

of a single dimple. The results in Fig. 13 show that the latter is the case.

There are small deviations, where the envelope of the colored lines does not coincide with the black line at larger pressures $p/p_c = 0.85$ in Fig. 13(b). The deviations at small $\Delta R^2$ are caused by the effect of unavoidable disclinations in the triangulation of the spherical surface. We use a triangulation that contains six four-fold disclinations (each carrying a topological charge of 2, producing an overall charge of 12), see Appendix B. Indentations interact with these disclinations and are initially formed at disclinations. Therefore, we observe six very shallow indentations which form at disclinations in the absence of a $z$-constraint along the black line, as also illustrated in Fig. 14. With increasing $\Delta R^2$ the system switches to a single indentation. The interaction of indentations with disclinations is stronger for large pressure.

There are also downward energy jumps for $p/p_c = 0.85$ in Fig. 13(b). These jumps are caused by large inward moves of a vertex in the center of the indentation when the indentation switches from its initial unstable convex shape into its final concave shape. For pressures $p/p_c \approx 0.5$, the constraint on the variance $\Delta R^2$ is not sufficient to suppress such sudden switches, eventually also as an effect of the existence of several small indentations because of the presence of disclinations, which affect $\Delta R^2$. Associated with this sudden switch is a hysteretic behavior if $\Delta R^2$ is reduced again starting from a concavely indented post-jump state. Then the capsule returns into its initial spherical shape along a different path of configurations with different energies as shown in Fig. 15 also for $p/p_c = 0.85$. The reverse deformation path exhibits a slightly smaller energy barrier. Despite the lower energy barrier, this deformation path has a steeper initial rise in energy when starting from the spherical shape, and is therefore not taken when the capsule is gradually indented. The energy barrier measured on the reverse path is only slightly lower, as the comparison in Fig. 16 shows, and will therefore have no significant influence on any of the previously discussed results.

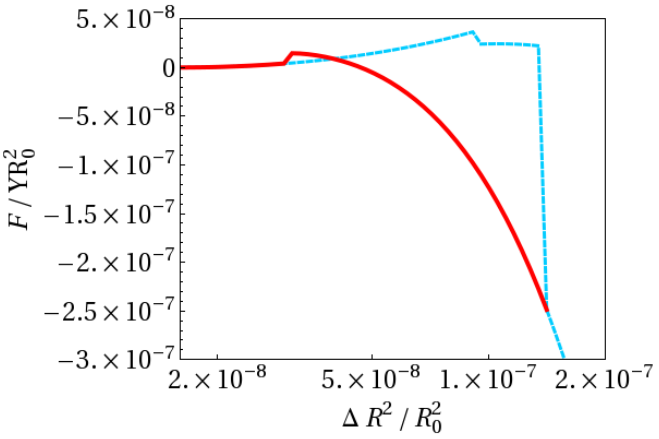


FIG. 15. Shape hysteresis and minimal enthalpy as a function of $\Delta R^2$. The light blue dashed line shows the minimum enthalpy for *increasing* $\Delta R^2$, starting from the spherical shape, and the dark red solid line shows the minimum enthalpy found for *decreasing* $\Delta R^2$, starting with a concavely indented shape. The reverse red path with concavely indented shapes exhibits a lower global enthalpy maximum than the blue forward path and becomes unstable for small $\Delta R^2$, where shapes become convex again.

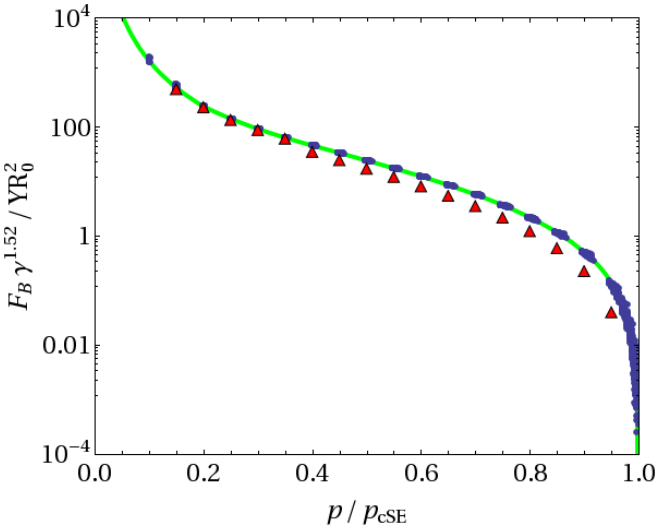


FIG. 16. Collapse of the energy barrier obtained by applying an additional $z$-constraint and for increasing $\Delta R^2$ (dots), numerical approximation of these values (line), and the slightly lower energy barrier (red triangles) obtained by reducing $\Delta R^2$ starting from a concave, indented shape.

For pressures that approach $p_c$, the paths with decreasing energy move closer to the energy maximum, as shown in Fig. 13(c).

Only if we further follow the system to much larger values of $\Delta R^2$ *behind* the energy barrier, multiple dimples are formed as shown in Fig. 12. These dimples start to form around the initial single dimple and spread over the entire sphere.

We conclude that single dimples appear to be stable *before* the energy barrier, i.e., as long as dimple formation still increases the enthalpy, whereas multiple dimples spread across the sphere *behind* the energy barrier where further dimple formation lowers the enthalpy again. Then the path with decreasing energy, along which multiple dimples can be formed, appears almost directly behind the energy maximum. This is consistent with the known behavior at the critical buckling pressure $p = p_c$. Then the energy maximum moves to $\Delta R^2 = 0$ and multiple dimples can immediately be formed [25].

## IV. CONCLUSIONS

Thermal fluctuations lead to a depression of the critical buckling pressure $p_c$ by two mechanisms: (i) parameter renormalization because of anharmonicities in normal displacement modes, which are mainly caused by the background curvature $1/R_0$ of the shell and (ii) thermal activation over the buckling barrier. In Ref. [45] the effects of parameter renormalization have already been considered; here we extended this approach to also take thermal activation into account.

The anharmonic coupling between different normal displacement modes leads to scale-dependent, renormalized elastic moduli $\kappa_R(q)$ and $Y_R(q)$, and also a scale-dependent pressure $p_R(q)$, which can be obtained from a RG transformation that has been derived in Ref. [45]. Buckling sets in if the two-point vertex function $D_R(q)$, which characterizes the curvature of the effective harmonic free enthalpy for the normal deformation mode $\tilde{f}(q)$, is renormalized to zero for a certain wave number $q = q^*$: $D_R(q^*) = 0$. The mode $\tilde{f}(q^*)$ then becomes unstable and initiates the buckling transition. This buckling criterion is slightly different from the buckling criterion $p_R(q^*)/p_{c,R}(q^*) = 1$, which is based on the renormalized ratio of pressure to critical buckling pressure that has been used in Ref. [45]. The resulting temperature-dependent critical buckling pressures are summarized in Fig. 3. The criterion $D_R(q^*) = 0$ gives a slightly higher value than obtained in Ref. [45].

The main conclusions regarding renormalization effects remain unchanged from Ref. [45]. Renormalization effects should be most pronounced for large dimensionless temperatures $\bar{T} = k_BT\sqrt{\gamma}/\kappa \sim (k_BT/\kappa)\sqrt{YR_0^2/\kappa}$ [see Eq. (20)]. For shells made from thin isotropically elastic materials this parameter becomes $\bar{T} \sim k_BTR_0/Eh^4$, which means that shells with large radius $R_0$ are more susceptible to thermal fluctuations. The relevance of thermal fluctuations depends most sensitively ($\bar{T} \propto h^4$) on shell thickness, and thin shells are most susceptible to thermal fluctuations.

For a typical soft material with $E \sim 0.1\,\mathrm{GPa}$, from

which a microcapsule of size $R_0 \sim 10\,\mu$m is synthesized, the shells should be ultrathin with $h \sim 1\,$nm to reach $\bar{T} \sim 400$. Also many biological capsules, such as red blood cells ($\bar{T} \sim 2-40$) or gram-negative bacteria ($\bar{T} \sim 8$) can exhibit fairly large $\bar{T}$. Moreover, $p_c(T)$ can, in principle, become negative also with the modified buckling criterion $D_R(q^*) = 0$, as Fig. 3 clearly shows. Therefore, a spontaneous buckling *without* external pressure but only caused by the fluctuation-generated pressure is possible as discussed in Ref. [45].

We extended the Pogorelov approximation and used numerical energy minimization with the Surface Evolver to quantify the energy barrier $F_{\rm B}(p)$ for a single axisymmetric dimple. We found a scaling behavior $F_{\rm B}(p) = YR_0^2 f_\nu(\nu)\gamma^{-\alpha} f_p\,(p/p_c)$ [see Eq. (30)] with an exponent $\alpha \simeq 3/2$ and a weak $\nu$-dependence $f_\nu(\nu) \approx 1$ in agreement with the Pogorelov approximation, i.e., $F_{\rm B}(p) \sim (Eh^4/R_0) f_p\,(p/p_c)$. We quantified the scaling function $f_p(x)$ numerically in Fig. 9 in excellent agreement with existing experimental data from Ref. [39]. A simple approximation is given by Eq. (33) with a pressure scaling function $f_p(x) \sim (1-x)^2 x^{-3}$, which is in agreement with the Pogorelov approximation $F_{\rm B} \propto p^{-3}$ for $x \ll 1$ and predicts that the barrier vanishes $F_{\rm B} \propto (1-p/p_c)^2$ close to the critical pressure. The exponent 2 is a numerical result and has to be corroborated by theoretical arguments in future research.

Considering a capsule or shell at half critical pressure $p = p_c/2$ (with $f_p(0.5) \sim 50$), we find $F_{\rm B}(p_c/2) \sim k_BT \sim 50/\bar{T}$ and the barrier height measured in thermal energy units is also governed by the dimensionless temperature $\bar{T}$. Instead of using the thermal energy scale $k_BT$, we can also use a mechanical energy scale and state that the characteristic size of the buckling barrier, $F_{\rm B}(p_c/2) \sim YR_0^2\gamma^{-3/2} \sim \kappa\gamma^{-1/2} \sim Eh^4/R_0$, is reduced over the elastic compression energy of the spherical shell just before buckling, $U_{\rm sph} \sim \kappa \sim Eh^3$, by a factor $\gamma^{-1/2} \sim h/R_0$.

For $p < p_c$ this energy barrier can be crossed by thermal activation on accessible time scales if $F_{\rm B} < k_BT$, which serves as criterion for thermal buckling via thermal activation. Thermal activation leads to a similar depression of $p_c(T)/p_c < 1$ as parameter renormalization. Both approaches give a critical pressure $p_c(T)/p_c$ which only depends on the dimensionless temperature $\bar{T}$. Finally, we combine parameter renormalization effects and thermal activation by using properly renormalized elastic parameters for the energy barrier. This leads to our final results in Fig. 11, which shows that thermal activation leads to a significant further decrease in $p_c(T)$ and cannot be neglected: for the relative difference $\Delta p_c(T)$ between the critical pressures from renormalization only and from thermal activation plus renormalization as compared to the zero temperature critical pressure $p_c(0)$ we find $|\Delta p_c(T)|/p_c(0) = 7,\ 11,\ 17,\ 27\%$ for dimensionless temperatures $\bar{T} = 1,\ 10,\ 100,\ 1000$.

Finally, we addressed the question to what extent buckling shapes with multiple dimples, which are known to govern the classical buckling instability at $p = p_c$, also play a role for the energy barrier for $p < p_c$ by constrained numerical energy minimization. In order to allow for the formation of multiple dimples we employed a constraint on the variance $\Delta R^2$ of the distance of vertices on the shell to the center of the shell. We compared with energy minimization where we constrain the distance of one vertex to the center, which only leads to formation of a single dimple. Our numerical results show that single dimples are stable *before* the energy barrier, whereas multiple dimples spread across the sphere *behind* the energy barrier when further dimple formation lowers the enthalpy again. Therefore, thermal activation at $p < p_c$ is governed by formation of a single indentation.

## ACKNOWLEDGMENTS

This research was supported in part by the National Science Foundation under Grant No. NSF PHY11-25915. We would also like to acknowledge useful discussions with Andrej Košmrlj.

### Appendix A: Renormalization group calculation

Following Košmrlj and Nelson [45], we re-derive the RG equations governing the scale-dependence of $\kappa_R(q)$, $p_R(q)$, and $Y_R(q)$.

For a momentum shell RG procedure we Fourier transform the effective enthalpy (11), which results in $F_{\rm eff} = F_0 + F_{\rm int}$ with a quadratic part

$$\frac{F_0}{A} = \sum_{\mathbf{q}} \frac{1}{2}\left[\kappa q^4 - \frac{pR_0q^2}{2} + \frac{Y}{R_0^2}\right]\tilde{f}(\mathbf{q})\tilde{f}(-\mathbf{q}) \qquad \text{(A1)}$$

and cubic and quartic interactions

$$\begin{aligned}\frac{F_{\rm int}}{A} = &\sum_{\substack{\mathbf{q}_1+\mathbf{q}_2=\mathbf{q}\neq 0\\ \mathbf{q}_3+\mathbf{q}_4=-\mathbf{q}\neq 0}} \frac{Y}{8}[q_{1i}P^T_{ij}(\mathbf{q})q_{2j}][q_{3i}P^T_{ij}(\mathbf{q})q_{4j}]\\ &\qquad\times\tilde{f}(\mathbf{q}_1)\tilde{f}(\mathbf{q}_2)\tilde{f}(\mathbf{q}_3)\tilde{f}(\mathbf{q}_4)\\ &+\sum_{\substack{\mathbf{q}_1\neq 0\\ \mathbf{q}_2+\mathbf{q}_3=-\mathbf{q}_1}} \frac{Y}{2R_0}[q_{2i}P^T_{ij}(\mathbf{q}_1)q_{3j}]\tilde{f}(\mathbf{q}_1)\tilde{f}(\mathbf{q}_2)\tilde{f}(\mathbf{q}_3),\end{aligned} \qquad \text{(A2)}$$

with $P^T_{ij}(\mathbf{q}) = \delta_{ij} - q_iq_j/q^2$. The normal displacements $\tilde{f}$ are separated into slow modes $\tilde{f}_<(\mathbf{x}) = \sum_{|\mathbf{q}|<\Lambda/b} e^{i\mathbf{q}\cdot\mathbf{x}}\tilde{f}(\mathbf{q})$ and fast modes $\tilde{f}_>(\mathbf{x}) = \sum_{|\mathbf{q}|>\Lambda/b} e^{i\mathbf{q}\cdot\mathbf{x}}\tilde{f}(\mathbf{q})$ containing modes with wave vectors smaller and larger than $\Lambda/b$, respectively.

Integrating out fast normal displacement modes $\tilde{f}(\mathbf{k})$ in the momentum shell $\Lambda/b < |\mathbf{k}| < \Lambda$ results in an effective enthalpy $F'_{\rm eff}[\tilde{f}_<] = -k_BT\ln\left(\int\mathcal{D}[\tilde{f}_>(\mathbf{x})]e^{-F_{\rm eff}/k_BT}\right)$, which only depends

on slow normal displacement modes with wave vectors $|\mathbf{q}| < \Lambda/b$,

$$F'_{\rm eff}[\{\mathbf{q}\}] = -k_BT \ln\left(\int \mathcal{D}[\tilde{f}(\mathbf{k})] e^{-(F_0[\{\mathbf{q},\mathbf{k}\}]+F_{\rm int}[\{\mathbf{q},\mathbf{k}\}])/k_BT}\right) = F_0[\{\mathbf{q}\}] - k_BT \ln \langle e^{-F_{\rm int}[\{\mathbf{q},\mathbf{k}\}]/k_BT}\rangle_{0,k}\,. \tag{A3}$$

The average $\langle ...\rangle_{0,k}$ is an average over fast modes with the quadratic part $F_0[\{k\}]$.

The logarithm can be expanded into cumulants, denoted by the superscript $(c)$,

$$F'_{\rm eff}[\{\mathbf{q}\}] = F_0[\{\mathbf{q}\}] + \sum_n \frac{(-1)^{n-1}}{n!(k_BT)^{n-1}} \langle (F_{\rm int}[\{\mathbf{q},\mathbf{k}\}])^n\rangle^{(c)}_{0,k}\,. \tag{A4}$$

The series can represented as Feynman diagrams leading to a systematic expansion in the number of loops. Up to one-loop order, all diagrams are shown in Fig. 17(c)-(i).

The single contributions of the Feynman diagrams shown in Fig. 17(c)-(i) to the effective energy (A4) to one-loop order are

$$\frac{F'_{\rm eff}[\{\mathbf{q}\}]_{(c)}}{A} = \sum_{\mathbf{q}} \frac{1}{2}\tilde{f}(\mathbf{q})\tilde{f}(-\mathbf{q}) \int_{\Lambda/b<|\mathbf{k}|<\Lambda} \frac{\mathrm{d}^2k}{(2\pi)^2} AYG\left(\mathbf{k}+\frac{\mathbf{q}}{2}\right)\left[q_iP^T_{ij}\left(\mathbf{k}-\frac{\mathbf{q}}{2}\right)\left(k_j+\frac{q_j}{2}\right)\right]^2, \tag{A5}$$

$$\begin{aligned}\frac{F'_{\rm eff}[\{\mathbf{q}\}]_{(d-g)}}{A} = &\sum_{\mathbf{q}} \frac{1}{2}\tilde{f}(\mathbf{q})\tilde{f}(-\mathbf{q}) \int_{\Lambda/b<|\mathbf{k}|<\Lambda} \frac{\mathrm{d}^2k}{(2\pi)^2} \frac{(-1)Y^2A^2}{k_BTR_0^2} G\left(\mathbf{k}+\frac{\mathbf{q}}{2}\right) G\left(\mathbf{k}-\frac{\mathbf{q}}{2}\right)\\ &\times\Bigg[\left[q_iP^T_{ij}\left(\mathbf{k}+\frac{\mathbf{q}}{2}\right)\left(k_j-\frac{q_j}{2}\right)\right]^2 - \left[q_iP^T_{ij}\left(\mathbf{k}-\frac{\mathbf{q}}{2}\right)\left(k_j+\frac{q_j}{2}\right)\right]\left[q_iP^T_{ij}\left(\mathbf{k}+\frac{\mathbf{q}}{2}\right)\left(k_j-\frac{q_j}{2}\right)\right]\\ &+2\left[q_iP^T_{ij}\left(\mathbf{k}-\frac{\mathbf{q}}{2}\right)\left(k_j+\frac{q_j}{2}\right)\right]\left[\left(k_i-\frac{q_i}{2}\right)P^T_{ij}(\mathbf{q})\left(k_j+\frac{q_j}{2}\right)\right] + \frac{1}{2}\left[\left(k_i-\frac{q_i}{2}\right)P^T_{ij}(\mathbf{q})\left(k_j+\frac{q_j}{2}\right)\right]^2\Bigg],\end{aligned} \tag{A6}$$

$$\begin{aligned}\frac{F'_{\rm eff}[\{\mathbf{q}\}]_{(h)}}{A} = &\sum_{\substack{\mathbf{q}\neq 0\\ \mathbf{q}_2+\mathbf{q}_3=-\mathbf{q}}} \frac{Y}{2R_0}\left[q_{2i}P^T_{ij}(\mathbf{q})q_{3j}\right]\tilde{f}(\mathbf{q})\tilde{f}(\mathbf{q}_2)\tilde{f}(\mathbf{q}_3)\\ &\times\int_{\Lambda/b<|\mathbf{k}|<\Lambda} \frac{\mathrm{d}^2k}{(2\pi)^2}\frac{(-1)YA^2}{2k_BT} G\left(\mathbf{k}+\frac{\mathbf{q}}{2}\right) G\left(\mathbf{k}-\frac{\mathbf{q}}{2}\right)\left[\left(k_i-\frac{q_i}{2}\right)P^T_{ij}(\mathbf{q})\left(k_j+\frac{q_j}{2}\right)\right]^2,\end{aligned} \tag{A7}$$

$$\begin{aligned}\frac{F'_{\rm eff}[\{\mathbf{q}\}]_{(i)}}{A} = &\sum_{\substack{\mathbf{q}_1+\mathbf{q}_2=\mathbf{q}\neq 0\\ \mathbf{q}_3+\mathbf{q}_4=-\mathbf{q}\neq 0}} \frac{Y}{8}[q_{1i}P^T_{ij}(\mathbf{q})q_{2j}][q_{3i}P^T_{ij}(\mathbf{q})q_{4j}]\tilde{f}(\mathbf{q}_1)\tilde{f}(\mathbf{q}_2)\tilde{f}(\mathbf{q}_3)\tilde{f}(\mathbf{q}_4)\\ &\times\int_{\Lambda/b<|\mathbf{k}|<\Lambda} \frac{\mathrm{d}^2k}{(2\pi)^2}\frac{(-1)YA^2}{2k_BT} G\left(\mathbf{k}+\frac{\mathbf{q}}{2}\right) G\left(\mathbf{k}-\frac{\mathbf{q}}{2}\right)\left[\left(k_i-\frac{q_i}{2}\right)P^T_{ij}(\mathbf{q})\left(k_j+\frac{q_j}{2}\right)\right]^2.\end{aligned} \tag{A8}$$

The relevant terms for the renormalization of $\kappa$, $p$, and $Y$ are terms of order $q^4$, $q^2$, and $q^0$ in Eqs. (A5) and (A6), respectively. They renormalize the quadratic part $F_0$ in (A1). The contributions to three- and four-point vertices (A7) and (A8) can also be used to calculate a renormalization of $Y$ in the cubic and quartic part $F_{\rm int}$ in (A2) by considering terms $q^0$.

After performing the momentum-shell integrals over $\Lambda/b < |\mathbf{k}| < \Lambda$ in (A5) and (A6) (approximating integrals over the momentum shell $\Lambda/b < |\mathbf{k}| < \Lambda$ as $\int_{\Lambda/b<|\mathbf{k}|<\Lambda} \mathrm{d}^2k g(\mathbf{k} \approx 2\pi g(\Lambda)\Lambda s$ for scale factors $b = e^s \approx 1 - s$ with $s \ll 1$) and after subsequent rescaling according to the equations 14 with $b = e^s$, we find new elastic parameters $\kappa'(s)$, $Y'(s)$, and $p'(s)$, that retain the form of the free enthalpy (11) upon a change of scale by a factor $b$. Their RG flow for an infinitesimal change of scale $b \approx 1 - ds$ is described by $\beta$-functions

$$\beta_\kappa = \frac{\mathrm{d}\kappa'}{\mathrm{d}s} = 2(\zeta_f - 1)\kappa' + \frac{3k_BTY'\Lambda^2}{16\pi D} - \frac{3k_BTY'^2\Lambda^2}{8\pi R_0'^2 D^2}\left[\frac{11}{12} + \frac{I_{\kappa 1}}{D^2} + \frac{I_{\kappa 2}}{D^4}\right], \tag{A9a}$$

$$\beta_Y = \frac{\mathrm{d}Y'}{\mathrm{d}s} = 2\zeta_f Y' - \frac{3k_BTY'^2\Lambda^6}{32\pi D^2}, \tag{A9b}$$

$$\beta_p = \frac{\mathrm{d}p'}{\mathrm{d}s} = (2\zeta_f + 1)p' + \frac{3k_BTY'^2\Lambda^4}{4\pi R_0'^3 D^2}\left[1 + \frac{I_p}{D^2}\right], \tag{A9c}$$

$$\beta_R = \frac{\mathrm{d}R_0'}{\mathrm{d}s} = -R_0', \tag{A9d}$$

with the denominator

$$D \equiv \kappa'\Lambda^4 - \frac{p'R_0'\Lambda^2}{2} + \frac{Y'}{R_0'^2}. \tag{A10}$$

Calculating $\beta$-functions for $Y$ using the three- and four-point vertices (A7) or (A8) yields the same $\beta_Y$, but with the terms $(3\zeta_f - 1)Y'$ or $(4\zeta_f - 2)Y'$ instead of $2\zeta_f Y'$ from a different rescaling. In order for all of these to produce the same result, $\zeta_f = 1$ has to be chosen.

The terms $I_{\kappa 1}$, $I_{\kappa 2}$, and $I_p$ in the RG equations (15) are

$$I_{\kappa 1} = \frac{1}{12}\left[3\frac{p'Y'}{R_0'} - p'^2R_0'^2\Lambda^4 - 16\frac{\kappa'Y'}{R_0'^2}\Lambda^4 + 7\kappa'p'R_0'\Lambda^6 - 8\kappa'^2\Lambda^8\right], \tag{A11a}$$

$$\begin{aligned} I_{\kappa 2} = \frac{1}{768}\Bigg[ &- \frac{24Y'^3\kappa'\Lambda^4}{R_0'^6} + \frac{Y'^2}{R_0'^4}(9p'^2R_0'^2\Lambda^4 - 76p'R_0'\kappa'\Lambda^6 + 268\kappa'^2\Lambda^8) \\ &+ \frac{Y'}{R_0'^2}(-5p'^3R_0'^3\Lambda^6 + 52p'^2R_0'^2\kappa'\Lambda^8 - 204p'R_0'\kappa'^2\Lambda^{10} + 160\kappa'^3\Lambda^{12}) \\ &+ (p'^4R_0'^4\Lambda^8 - 12p'^3R_0'^3\kappa'\Lambda^{10} + 56p'^2R_0'^2\kappa'^2\Lambda^{12} - 96p'R_0'\kappa'^3\Lambda^{14} + 60\kappa'^4\Lambda^{16})\Bigg], \end{aligned} \tag{A11b}$$

$$I_p = \frac{1}{48}\left[\frac{Y'}{R_0'^2}(3p'R_0'\Lambda^2 - 16\kappa'\Lambda^4) + (-p'^2R_0'^2\Lambda^4 + 7p'R_0'\kappa'\Lambda^6 - 8\kappa'^2\Lambda^8)\right]. \tag{A11c}$$

The function $\beta_\kappa$ in (A9) slightly differs from the results in Ref. [45]. Differences are in the two terms $(3k_BTY'^2\Lambda^2/8\pi R_0^2D^2)\left(\frac{11}{12} + \frac{I_{\kappa 1}}{D^2}\right)$ in Eq. (A9a) for the function $\beta_\kappa$. First, the function $I_{\kappa 1}$ in (A11a) differs from the corresponding function in Ref. [45]; secondly the factor 11/12 is unity in Ref. [45]. Both differences exactly compensate each other such that we have the exact same RG equations as in Ref. [45].

The scale-dependent, i.e., renormalized but unrescaled quantities $\kappa_R(q)$, $p_R(q)$, and $Y_R(q)$ defined via Eq. (17) obey RG equations

$$\begin{aligned} -q\frac{\mathrm{d}\kappa_R}{\mathrm{d}q} = &\frac{3k_BTY_Rq^2}{16\pi D_R} \\ &- \frac{3k_BTY_Rq^2}{8\pi R_0^2D_R^2}\left[\frac{11}{12} + \frac{I_{\kappa 1}}{D_R^2} + \frac{I_{\kappa 2}}{D_R^4}\right], \end{aligned} \tag{A12a}$$

$$-q\frac{\mathrm{d}Y_R}{\mathrm{d}q} = -\frac{3k_BTY_R^2q^6}{32\pi D_R^2}, \tag{A12b}$$

$$-q\frac{\mathrm{d}p'}{\mathrm{d}q} = \frac{3k_BTY_R^2q^4}{4\pi R_0^3D_R^2}\left[1 + \frac{I_p}{D_R^2}\right], \tag{A12c}$$

with $D_R(q) = \kappa_R(q)q^4 - p_R(q)R_0q^2/2 + Y_R(q)/R_0^2$ as in Eq. (18) and terms $I_{\kappa 1}$, $I_{\kappa 2}$, and $I_p$ which are given by Eq. (A11), where we similarly replace $\kappa' \to \kappa_R$, $Y' \to Y_R$, $p' \to p_R$, $R_0' \to R_0$, and $\Lambda \to q$.

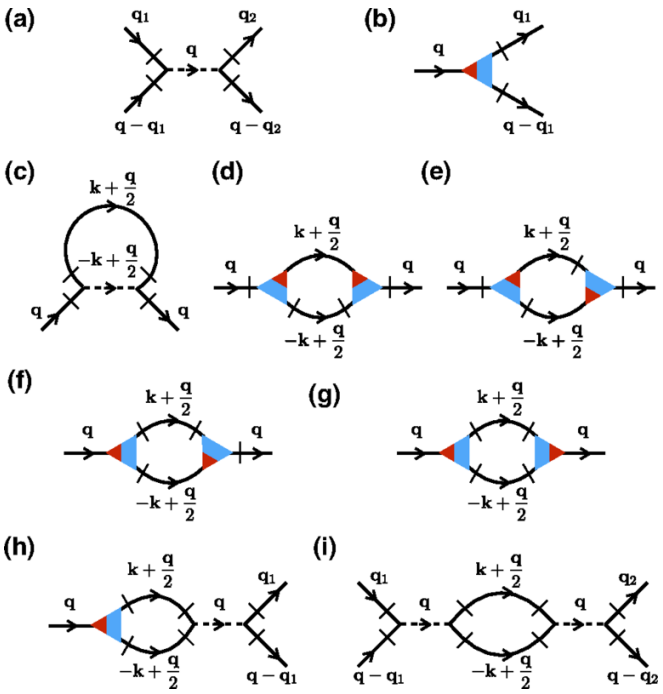


FIG. 17. Feynman diagrams approximating (A4) to one-loop order. The legs correspond to $\tilde{f}(\mathbf{q})$, legs with slashes correspond to derivatives of $\tilde{f}(\mathbf{q})$, i.e., $q_i\tilde{f}(\mathbf{q})$. Connected legs represent the propagator $G(\mathbf{q})$. The blue parts of the three-point vertices connect to the derivatives, whereas the red parts connect to legs without slashes. Three-point vertices carry the factor $Y/R_0$, and four-point vertices carry the factor $Y$. Image taken from [45].

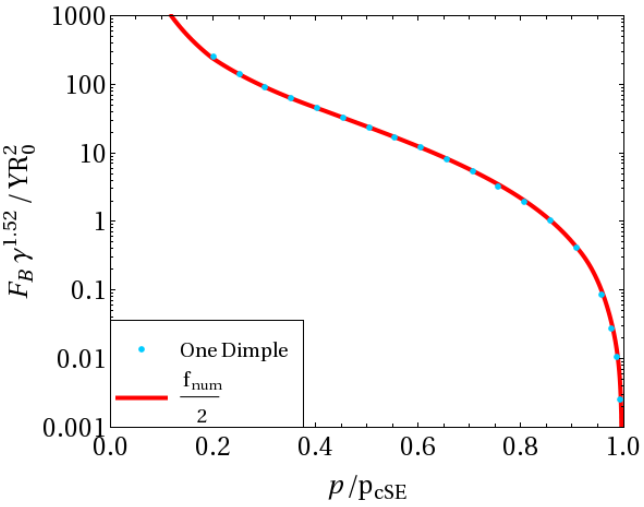


FIG. 18. Energy barrier as a function of pressure for one dimple (light blue points), and half of the approximated energy barrier for two dimples (solid dark red line) from numerical simulations, see Eq. (B1) (for $\gamma = 10^4$ and $\nu = 0.3$).

### Appendix B: Energy minimization using the Surface Evolver

The Surface Evolver is a program developed by Brakke for calculating the lowest-energy shape of a triangulated surface with definable energies and constraints [50]. The surface consists of vertices, which are connected by edges, which in turn form facets. After specifying the energy functional, the minimal energy shape is found iteratively by displacing vertices either following the steepest gradient or with more refined conjugate gradient methods and according to the applied constraints.

In order to create a sphere in the Surface Evolver, a cube is created first. This surface is successively refined by dynamical triangulation using a simple liquid surface energy $E = \sigma \int \mathrm{d}S$ with constant surface tension $\sigma$ until an acceptable spherical shape is reached. Therefore, the resulting final triangulation contains six four-fold disclinations corresponding to the six faces of the original cube. Once this has been accomplished, the surface tension is set to zero, the triangulation is fixed, and the appropriate dimensionless elastic energies (21) are activated (i.e., we measure energies in units of $YR_0^2$ and lengths in units of $R_0$ in the simulation); the newly created sphere is defined as the relaxed state of the surface in the elastic energies (21).

The elastic energies are then minimized for a given dimensionless pressure $p$ (measured in units of $R_0/Y$). We determine the barrier for $0 < p \leq p_c$, where the sphere first compresses uniformly. Then we map out the energy landscape of the buckling energy barrier by selecting two vertices on opposite sides of the compressed sphere of radius $R(p) < R_0$, which are fixed in place with a distance $z_0 = 2R(p)$. By keeping a constraint on the distance $z$ between these two vertices and decreasing this distance $z$ starting from $z_0$, we control the size of the dimple. A similar procedure has been used in Ref. [44] for fluctuating spherical shells. We obtain the enthalpy $F = F(z)$ as a function of $z$ for a given pressure $p$ (see Fig. 8) and can determine its maximum $F_{\max}$. The energy barrier is $F_\mathrm{B} = F_{\max} - F(z = z_0)$ with $z_0 = 2R(p)$. By changing the pressure $p$ we can numerically determine the energy barrier as a function of pressure $F_\mathrm{B} = F_\mathrm{B}(p)$.

Constraining the distance $z$ between two opposite points on the sphere generates two dimples upon decreasing $z$; if one of the points is fixed before decreasing $z$, only a single dimple is created. For sufficiently small dimples, the energy barrier for a sphere that forms only one dimple is half of the energy barrier for a sphere with two dimples [40], because the interaction of two small dimples on opposite sides of a sphere can be neglected, see Fig. 18.

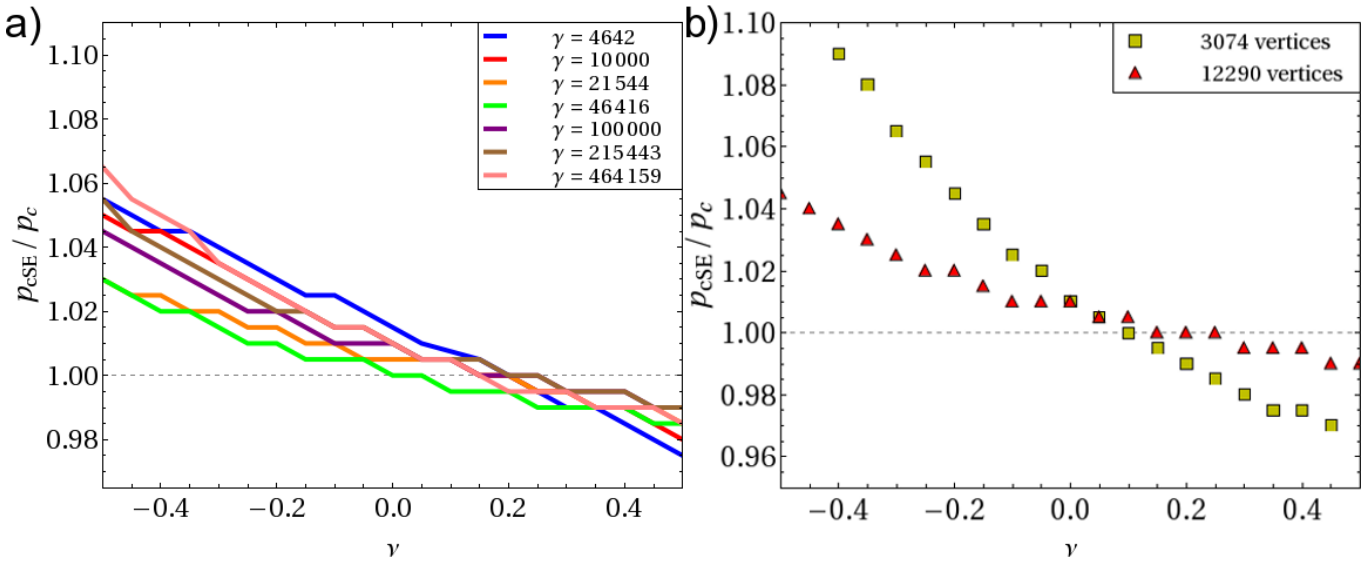


FIG. 19. Approximate critical buckling pressure $p_{c,SE}$ as determined with the Surface Evolver as a function of Poisson's number $\nu$ (a) for different values of $\gamma$ with 12290 vertices and (b) for different vertex counts at $\gamma = 100000$. For $\nu \approx 0.15$, $p_{c,SE}$ roughly agrees with $p_c$. Therefore, and because the estimate $p_{c,SE}$ for the critical buckling pressure becomes more inaccurate for larger $\nu$ (as the Surface Evolver does not reach the buckled shape in a reasonable amount of computation time even for $p > p_{c,SE}$), Poisson ratios $\nu = 0.05...0.5$ are used for the numerical calculations. For larger vertex counts the approximate critical buckling pressure moves towards $p_c$, indicating that the deviation is mostly a triangulation effect. However, disclinations most likely also play a role. A vertex count of 12290 was used for all remaining numerical simulations.

### 1. Discretization effects

In simulating buckling, discretization effects occur for the triangulated surfaces in the Surface Evolver. In the Surface Evolver buckling does not occur exactly at the classical buckling pressure $p_c = 4(Y/R_0)\gamma^{-1/2}$ but at an approximate value $p_{c,SE}$, which deviates because of discretization effects. This value is determined numerically by gradually increasing the pressure until the average of all vertex distances to the sphere's center becomes smaller than $0.9 \cdot R_0$, at which point buckling has occurred. This approximated buckling pressure $p_{c,SE}$ is shown in Fig. 19 for different Poisson ratios $\nu$ and different triangulations. In order to obtain an energy barrier $F_B(p/p_c)$, which properly vanishes at $p = p_c$, i.e., $F_B(1) = 0$, we use the numerically determined buckling pressure $p_{c,SE}$ instead of $p_c$. We analyze the numerical results for the energy barrier in Figs. 9, 10, and 20 also as a function of $p/p_{c,SE}$ rather than $p/p_c$.

### 2. Numerical approximation for the energy barrier

A very accurate approximation for the numerically determined energy barrier of two dimples can be given as

$$\frac{2F_{B,num}(p/p_c,\nu,\gamma)}{YR_0^2} = 2f_\nu(\nu)\gamma^{-1.52}f_{p,num}(p/p_c) \quad \text{(B1)}$$

with a scaling function

$$2f_{p,num}(x) = \begin{cases} f_1(x) & x > 0.910 \\ f_2(x) & 0.910 > x > 0.418 \\ f_3(x) & 0.418 > x > 0.198 \\ f_4(x) & 0.198 > x \end{cases} \quad \text{(B2)}$$

with

$$
\begin{aligned}
f_1(x) &= -8490.551 - 12199.07\exp(-0.07155726x) + 4504.429/x^6 \\
&\quad - 10596.10/x^5 - 619.6270/x^4 + 9590.704/x^3 + 7692.978/x^2 \\
&\quad - 2309.406/x + 1804.463x + 18542.43x^2 - 8762.693x^3, \\
f_2(x) &= -74.00287 - 691.7514\exp(-1.026248x) + 0.01542655/x^6 \\
&\quad + 0.005939230/x^5 - 0.5782996/x^4 + 12.10501/x^3 - 83.49014/x^2 \\
&\quad + 389.3926/x + 6.859172x - 0.7489285x^2 - 1.683589x^3, \\
f_3(x) &= -9.090486 + 12.55716/x^{2.272675}, \\
f_4(x) &= 20.05584 + 4.911410/x^{2.815042},
\end{aligned}
\tag{B3}
$$

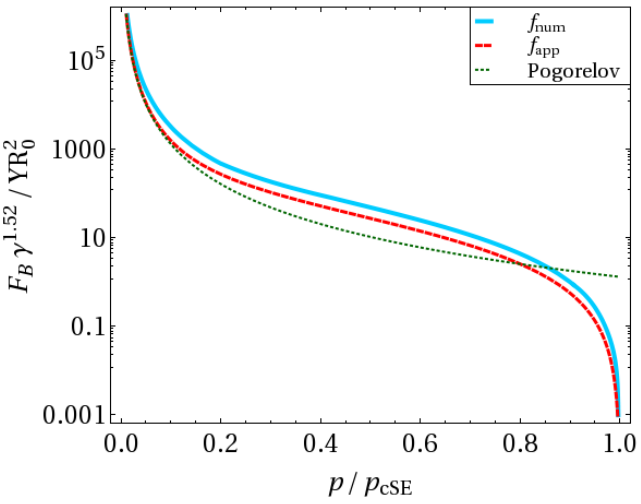


FIG. 20. Energy barrier for a sphere with one dimple as a function of pressure (for $\gamma = 10^4$ and $\nu = 0.3$) as obtained from numerical simulations [Eq. (B1), light blue solid line], from the Pogorelov model [Eq. (29), green dotted line], and according to the approximation (B5) (dark red dashed line).

and

$$
f_\nu(x) = 0.9754744 + 0.08569536\nu. \tag{B4}
$$

The $\nu$-dependence is very weak.

A simpler approximation formula, which is motivated by the Pogorelov result (29), is

$$
\begin{aligned}
&\frac{F_{\rm B,num}(p/p_c,\gamma)}{YR_0^2} = \gamma^{-3/2} f_{\rm p,app}(p/p_c) \quad \text{with} \\
&\qquad f_{\rm p,app}(x) = 1.44\,(1-x)^2(x^{-3} + 34.1\,x^{-1}).
\end{aligned}
\tag{B5}
$$

This simple approximation agrees within 20% with Eq. (B1) (see Fig. 20).


[1] G. Lim H. W., M. Wortis, and R. Mukhopadhyay, in *Soft Matter Vol. 4: Lipid Bilayers and Red Blood Cells*, edited by G. Gompper and M. Schick (Wiley-VCH Verlag GmbH & Co. KGaA, Weinheim, 2008) Chap. 2.
[2] S. Boey, D. Boal, and D. Discher, Biophys. J. **75(3)** (1998).
[3] M. Buenemann and P. Lenz, Proc. Natl. Acad. Sci. U.S.A **104**, 9925 (2007).
[4] J. Michel, I. Ivanovska, M. Gibbons, W. Klug, C. Knoler, G. Wuite, and C. Schmidt, Proc. Natl. Acad. Sci. U.S.A **103(16)** (2006).
[5] E. Katifori, S. Alben, E. Cerda, D. R. Nelson, and J. Dumais, Proc. Natl. Acad. Sci. U.S.A **107(17)** (2010).
[6] E. Donath, G. Sukhorukov, F. Caruso, S. Davis, H. Möhwald, H. Lichtenfeld, and V. Popov, Polym. Adv. Technol. **9(10-11)** (1998).
[7] W. Meier, Chem. Soc. Rev. **29(5)** (2000).
[8] H. N. Yow and A. F. Routh, Soft Matter **2(11)** (2006).
[9] B. F. Gibbs, S. Kermasha, I. Alli, and C. N. Mulligan, Int. J. Food Sci. Nutr. **50(3)** (1999).
[10] K. Miyazawa, I. Yajima, I. Kaneda, and T. Yanaki, J. Cosm. Sci. **51** (2000).
[11] Y. Zhang, H. Chan, and K. Leong, Adv. Drug Deliv. Rev. **65(1)** (2013).
[12] W. H. D. Jong and P. J. A. Borm, Int. J. Nanomed. **3** (2008).
[13] L. D. Landau and J. M. Lifshitz, *Theory of Elasticity* (Pergamon Press, 1970).
[14] A. Libai and J. G. Simmonds, *The Nonlinear Theory of Elastic Shells* (Cambridge University Press, 1998).

[15] A. Lazarus, H. C. B. Florijn, and P. M. Reis, Phys. Rev. Lett. **109**, 144301 (2012).

[16] D. Vella, A. Ajdari, A. Vaziri, and A. Boudaoud, Phys. Rev. Lett. **109**, 144302 (2012).

[17] S. Timoshenko and J. Gere, *Theory of Elastic Stability* (Tata McGraw-Hill Education, 1961).

[18] C. Gao, Eur. Phys. J. E **5**, 21 (2001).

[19] A. Fery, F. Dubreuil, and H. Möhwald, New J. Phys. **6**, 18 (2004).

[20] S. Sacanna, W. T. M. Irvine, L. Rossi, and D. J. Pine, Soft Matter **7**, 1631 (2011).

[21] S. S. Datta, S.-H. Kim, J. Paulose, A. Abbaspourrad, D. R. Nelson, and D. A. Weitz, Phys. Rev. Lett. **109**, 134302 (2012).

[22] A. V. Pogorelov, *Bendings of Surfaces and Stability of Shells* (In: *Translations of Mathematical Monographs Vol. 72*. American Mathematical Society, 1988).

[23] R. Zoelly, *Über ein Knickungsproblem an der Kugelschale* (Ph.D. thesis, ETH Zürich, 1915).

[24] E. Ventsel and T. Krauthammer, *Thin Plates and Shells* (CRC Press, 2001).

[25] J. W. Hutchinson, J. Appl. Mech. **34**, 49 (1967).

[26] W. Koiter, Proc. Kon. Nederl. Akad. Wet. Amsterdam B **72**, 40 (1969).

[27] R. L. Carlson, R. L. Sendelbeck, and N. J. Hoff, Exp. Mech. **7(7)** (1967).

[28] J. Paulose and D. R. Nelson, Soft Matter **9**, 8227 (2013).

[29] S. Knoche and J. Kierfeld, Phys. Rev. E **84**, 046608 (2011).

[30] S. Knoche and J. Kierfeld, Soft matter **10**, 8358 (2014).

[31] C. Quilliet, Eur. Phys. J. E **35**, 48 (2012).

[32] S. Knoche and J. Kierfeld, Eur. Phys. J. E **37**, 62 (2014).

[33] S. Knoche and J. Kierfeld, EPL **106**, 24004 (2014).

[34] J. W. Hutchinson and J. M. T. Thompson, Phil. Trans. R. Soc. A **375**, 20160154 (2017).

[35] A. Y. Evkin and O. V. Lykhachova, Int. J. Solids Struct. **118-119**, 14 (2017).

[36] The classical buckling pressure $p_c$ was denoted by $p_{\mathrm{cb}}$ and the critical pressure for equal energies by $p_c$ in Refs. [29, 30] or $p_{1\mathrm{st}}$ in Refs. [32, 33].

[37] S. Knoche, *Instabilities and shape analyses of elastic shells* (Ph.D. thesis, TU Dortmund, 2014).

[38] A. Y. Evkin and A. L. Kalamkarov, Int. J. Solids Struct. **38**, 8975 (2001).

[39] J. Marthelot, F. López Jiménez, A. Lee, J. W. Hutchinson, and P. M. Reis, J. Appl. Mech. **84**, 121005 (2017).

[40] J. W. Hutchinson and J. M. T. Thompson, J. Appl. Mech. **84**, 061001 (2017).

[41] J. M. T. Thompson, J. W. Hutchinson, and J. Sieber, Int. J. Bifurc. Chaos **27**, 1730048 (2017).

[42] E. Virot, T. Kreilos, T. M. Schneider, and S. M. Rubinstein, Phys. Rev. Lett. **119**, 224101 (2017).

[43] F. Ahmadpoor and P. Sharma, Extreme Mech. Lett. **14**, 38 (2017).

[44] J. Paulose, G. A. Vliegenthart, G. Gompper, and D. R. Nelson, Proc. Natl. Acad. Sci. U.S.A **109**, 19551 (2012).

[45] A. Košmrlj and D. R. Nelson, Phys. Rev. X **7**, 011002 (2017).

[46] W. Helfrich, Z. Naturforsch. C **28(11)** (1973).

[47] D. R. Nelson, T. Piran, and S. Weinberg, *Theory of the crumpling transition. Statistical Mechanics of Membranes and Surfaces*, 2nd edition (World Scientific, Singapore, 2004).

[48] Note that Pogorelov used a slightly different form of the bending energy in Ref. [22] which included a Poisson number $\nu$ to account for an anisotropy of bending deformations. The Helfrich energy corresponds to $\nu = 1$. This difference has practically no effect on our results.

[49] M. Gomez, D. E. Moulton, and D. Vella, Proc. Royal Soc. A **472**, 20150732 (2016).

[50] K. A. Brakke, Exp. Math. **1** (1992).

[51] J. A. Aronovitz and T. C. Lubensky, Phys. Rev. Lett. **60**, 2634 (1988).